

A burst in a wind bubble and the impact on baryonic ejecta: high-energy gamma-ray flashes and afterglows from fast radio bursts and pulsar-driven supernova remnants

Kohta Murase¹, Kazumi Kashiyama², and Peter Mészáros¹

¹*Center for Particle and Gravitational Astrophysics; Department of Physics; Department of Astronomy & Astrophysics, The Pennsylvania State University, University Park, PA 16802, USA*

²*Einstein Fellow – Theoretical Astrophysics Center, Department of Astronomy, University of California, Berkeley, CA 94720, USA*

Submitted to arXiv: 28 March 2016

ABSTRACT

Tenuous wind bubbles, which are formed by the spin-down activity of central compact remnants, are relevant in some models of fast radio bursts (FRBs) and superluminous supernovae. We study their high-energy signatures, focusing on the role of pair-enriched bubbles produced by young magnetars, rapidly-rotating neutron stars, and magnetized white dwarfs. (i) First, we study the nebular properties and the conditions allowing for escape of high-energy gamma-rays and radio waves, showing that their escape is possible for nebulae with ages of $\gtrsim 10 - 100$ yr. In the rapidly-rotating neutron star scenario, we find that radio emission from the quasi-steady nebula itself may be bright enough to be detected especially at sub-mm frequencies, which is relevant as a possible counterpart of pulsar-driven SNe and FRBs. (ii) Second, we consider the fate of bursting emission in the nebulae. We suggest that an impulsive burst may lead to a highly relativistic flow, which would interact with the nebula. If the shocked nebula is still relativistic, pre-existing non-thermal particles in the nebula can be significantly boosted by the forward shock, leading to short-duration (maybe millisecond or longer) high-energy gamma-ray flashes. Possible dissipation at the reverse shock may also lead to gamma-ray emission. (iii) After such flares, interactions with the baryonic ejecta may lead to afterglow emission with a duration of days to weeks. In the magnetar scenario, this burst-in-bubble model leads to the expectation that nearby ($\lesssim 10 - 100$ Mpc) high-energy gamma-ray flashes may be detected by the High-Altitude Water Cherenkov Observatory and the Cherenkov Telescope Array, and the subsequent afterglow emission may be seen by radio telescopes such as the Very Large Array. (iv) Finally, we discuss several implications specific to FRBs, including constraints on the emission regions and limits on soft gamma-ray counterparts.

Key words: non-thermal—fast radio bursts—supernovae

1 INTRODUCTION

Fast radio bursts (FRBs) are a new class of transients discovered in the last decade (Lorimer et al. 2007; Keane et al. 2012; Thornton et al. 2013; Burke-Spolaor & Bannister 2014; Spitler et al. 2014; Ravi, Shannon & Jameson 2015; Petroff et al. 2015; Masui et al. 2015; Champion et al. 2015). They are very short ($\sim 1 - 10$ ms) and bright ($\sim 0.1 - 1$ Jy) sporadic events observed in the ~ 1 GHz bands showing a large dispersion measure (DM), $DM \sim 500 - 1000$ pc cm⁻³. If the dispersion originates mainly from the intergalactic propagation (Ioka 2003; Inoue 2004),

the sources can be at cosmological distance up to $z \sim 1$ (but see, e.g., Loeb, Shvartzvald & Maoz 2014; Maoz et al. 2015), and a high brightness temperature requires a coherent emission mechanism (e.g., Lorimer et al. 2007; Lyubarsky 2008; Thornton et al. 2013; Katz 2014). Interestingly, despite being relatively common (~ 10 % of core-collapse supernovae; Thornton et al. 2013; Keane & Petroff 2015; Law et al. 2015), the origin of FRBs is still unknown.

Various possibilities for the progenitors of FRBs have been proposed (see, e.g., Kulkarni et al. 2014, and references therein). Among them, extragalactic young neutron stars (NSs) including strongly magne-

tized NSs (so-called magnetars) have been considered as promising candidates (Popov & Postnov 2010; Lyubarsky 2014; Falcke & Rezzolla 2014; Cordes & Wasserman 2016; Connor, Sievers & Pen 2016). NSs are expected to form as compact remnants of core collapse supernova (SN) explosions, and a significant fraction of the magnetic energy and/or rotation energy can be extracted from the young NSs whose magnetic fields have not decayed yet. Compact merger models are also often discussed, where either NS or white dwarf (WD) or black hole (BH) are involved in the merger system (Totani 2013; Zhang 2014; Kashiyama, Ioka & Mészáros 2013). For NS-NS, NS-BH, and WD-WD mergers, baryonic ejecta with $\sim 10^{-5} - 10^{-2} M_{\odot}$ are expected to move with a fast velocity of $\sim 0.05 - 0.3 c$.

In either case, one naturally expects the formation of a tenuous wind bubble embedded in the baryonic ejecta, and the relativistic wind is driven by the spin-down activity of the NSs or WDs. It has been thought that pulsar winds that are initially Poynting-dominated become relativistic by the time they reach the light cylinder, and may further be accelerated in the wind zone via magnetic dissipation processes (e.g., Komissarov 2013, and references therein). Studies of Galactic pulsar wind nebulae (often referred to as plerions) suggest that a significant fraction of the spin-down energy is dissipated at the termination shock, where it converts into the non-thermal energy of accelerated particles, which are primarily electrons and positrons (Rees & Gunn 1974; Kennel & Coroniti 1984). Embryonic nebular emission has also been of interest in the literature of gamma-ray bursts (GRBs) (e.g., Usov 1992; Thompson 1994; Blackman & Yi 1998; Dai & Lu 1998; Zhang & Mészáros 2001) including the ‘‘supranova’’ model (e.g., Vietri & Stella 1998; Inoue, Guetta & Pacini 2003), energetic SNe such as super-luminous SNe (SLSNe) (e.g., Thompson, Chang & Quataert 2004; Maeda et al. 2007; Kasen & Bildsten 2010; Woosley 2010; Murase et al. 2015; Kashiyama et al. 2016), and kilonovae/macronovae (e.g., Kisaka, Ioka & Takami 2015; Gao et al. 2015; Kisaka, Ioka & Nakar 2016). An efficient conversion of the rotation energy into particle energy is required for the pulsar-driven SN model to explain these energetic SNe.

In this work, we study the consequences of an impulsive burst that occurs inside a wind bubble and SN ejecta. Multi-wavelength observations are crucial for distinguishing among the various models, and here we show that the existence of wind bubbles leads to interesting implications for the observations. We investigate three representative cases as examples, (a) the magnetar scenario, (b) the rapidly-rotating neutron star (RNS) scenario, and (c) the magnetized white dwarf (MWD) scenario. In Section 2 we outline our goals and we set up a model of the nebula emission based on the theoretical modeling of Galactic pulsar wind nebulae. Then, independently of the details of the emission mechanisms, we consider the fate of high-energy gamma-rays and radio waves propagating in the nebula and in the baryonic ejecta, and show that the escape of gamma-rays and radio waves is possible for NSs with ages of $T \gtrsim 10 - 100$ yr. In Section 3, we discuss the impact of a highly relativistic outflow that originates from an impulsive magnetic dissipation event. The de-

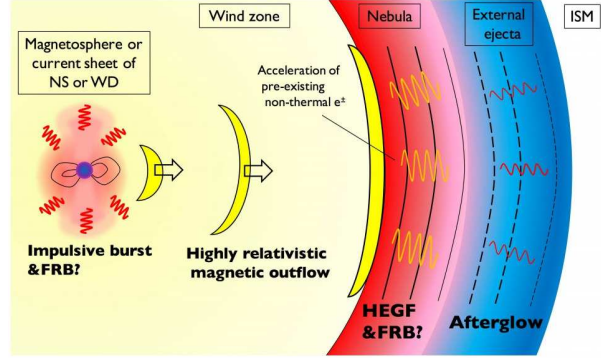


Figure 1. Schematic picture of the burst-in-bubble model.

celerating relativistic flow may boost the pre-existing non-thermal particles in the nebula, and high-energy gamma-ray flashes (HEGFs) are expected in the GeV-TeV range. We also argue that possible dissipation at the reverse shock leads to lower-energy gamma-ray emission in the MeV-GeV range. In Section 4, we discuss the possibility of a subsequent afterglow emission, and show that interactions with the dense baryonic ejecta may lead to detectable radio emission for nearby bursts, especially in the magnetar scenario. In Section 5, we discuss possible constraints on the magnetar giant flare scenario, as well as some issues arising in merger scenarios. Throughout this work, we use the notation $Q = 10^x Q_x$ in CGS unit unless noted otherwise.

2 SETUP: PROPERTIES OF WIND BUBBLES

2.1 Simplified nebula dynamics

We consider young nebulae that are formed by the spin-down activity of NSs (or WDs) embedded in the SN ejecta (or merger ejecta). Such a scenario is naturally expected in many models involving nascent pulsars and MWs¹, for not only FRBs but also SLSNe, GRBs, kilonovae/macronovae, high-energy neutrino emitters (e.g., Murase, Mészáros & Zhang 2009; Fang et al. 2014), and even TeV cosmic-ray electron-positron factories (Kashiyama, Ioka & Kawanaka 2011), although reference parameters vary among the scenarios (see Fig. 6). The nebular emission is powered by the rotation energy, whose energy budget is given by

$$\begin{aligned} \mathcal{E}_{\text{rot}} &= \frac{1}{2} I \Omega_i^2 \\ &\simeq \begin{cases} 1.9 \times 10^{47} \text{ erg } M_{*,\text{Ch}} R_{*,6}^2 P_{i,-0.5}^{-2} & (\text{magnetar}) \\ 1.9 \times 10^{52} \text{ erg } M_{*,\text{Ch}} R_{*,6}^2 P_{i,-3}^{-2} & (\text{RNS}) \\ 3.5 \times 10^{49} \text{ erg } M_{*,1M_{\odot}} R_{*,8.7}^2 P_{i,1}^{-2} & (\text{MWD}) \end{cases} \quad (1) \end{aligned}$$

where $I \approx 0.35 M_* R_*^2$ is the moment of inertia. Hereafter, we consider $M_* \approx M_{\text{Ch}} = 1.4 M_{\odot}$ (where M_{Ch} is the Chandrasekhar mass) and $R_* \approx 10^6$ cm for NSs, whereas we adopt

¹ Of course, there are exceptions. For example, if NSs or magnetars are formed by the accretion-induced collapse, we do not have to expect the existence of the dense SN ejecta.

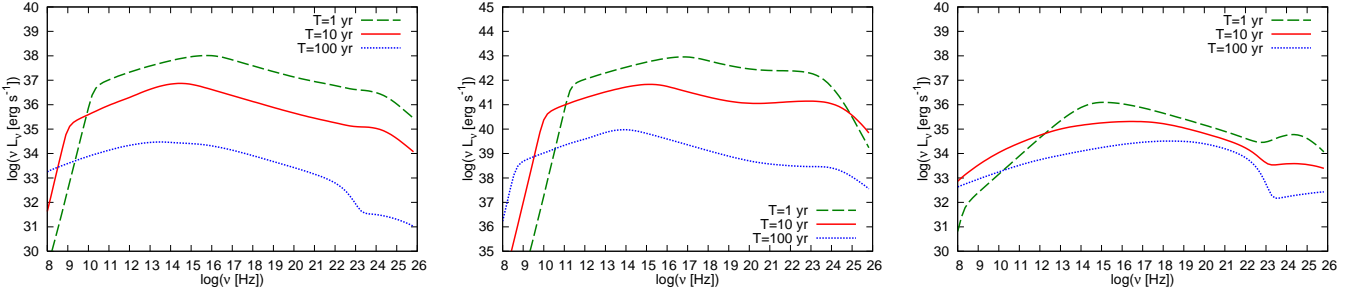


Figure 2. Spectra of a very young nebula in the magnetar scenario (left panel), RNS scenario (middle panel), and MWD scenario (right panel). Numerical calculations are performed based on Murase et al. (2015). Effects of attenuation in the ejecta are not shown (see text). The microphysical parameters are set to $\epsilon_B = 0.01$, $\epsilon_e = 1 - \epsilon_B$, $\gamma_b = 10^5$, $q_1 = 1.5$, $q_2 = 2.5$, and the parameters related to the dynamics are given in the text.

$M_* \approx 1.0 M_\odot$ and $R_* \approx 10^{8.7}$ cm for WDs. (For the rest of our discussion in Section 2.1, we do not show the explicit dependence on R_* .) Note that $\Omega_i = 2\pi/P_i$ is the rotation frequency at the birth of the compact object. For Galactic pulsars, the typical value of the initial period at the birth is estimated to be $P_i \sim 300$ ms (Faucher-Giguère & Kaspi 2006), which is used for the magnetar scenario. Note that the period becomes $P(T) \gtrsim 5$ s after 1000 yr. We consider $P_i = 10^{-3}$ s in the RNS scenario, and $P_i = 10$ s in the MWD scenario.

Based on recent magnetohydrodynamics simulations (Gruzinov 2005; Spitkovsky 2006; Tchekhovskoy, Spitkovsky & Li 2013), the initial spin-down power is

$$L_{\text{sd},i} \approx \frac{B_*^2 R_*^6 (2\pi/P_i)^4}{4c^3} (1 + \sin^2 \chi) \approx \begin{cases} 2.4 \times 10^{39} \text{ erg s}^{-1} B_{*,15}^2 P_{i,-0.5}^{-4} & (\text{magnetar}) \\ 2.4 \times 10^{44} \text{ erg s}^{-1} B_{*,12.5}^2 P_{i,-3}^{-4} & (\text{RNS}) \\ 3.8 \times 10^{37} \text{ erg s}^{-1} B_{*,9}^2 P_{i,1}^{-4} & (\text{MWD}) \end{cases} \quad (2)$$

where χ is the angle between the rotation and magnetic axes, and numerical values are obtained with $\langle \sin^2 \chi \rangle = 2/3$. Nominal magnetic field strengths are set to $B_* \sim 10^{15}$ G in the magnetar scenario, $B_* \sim 10^{12.5}$ G in the RNS scenario, and $B_* \sim 10^9$ G in the MWD scenario. Note that the magnetar scenario may include the magnetar hyperflare model for FRBs (Popov & Postnov 2010; Lyubarsky 2014), although the association of soft gamma-ray emission depends on its dissipation mechanisms. The RNS scenario may include the blitzar model and other models motivated by giant pulses from the Crab pulsar (Falcke & Rezzolla 2014; Cordes & Wasserman 2016). The MWD scenario is a new possibility considered in this work. Note that this MWD scenario is different from the WD-WD merger model of FRBs (Kashiyama, Ioka & Mészáros 2013) in the sense that the magnetic dissipation occurs much later than the MWD birth². In the MHD approximation, the spin-down power is significant even for aligned rotators with $\chi = 0$,

² In Kashiyama, Ioka & Mészáros (2013), FRB emission is expected to occur in a polar region, where the ambient density could be small enough.

where the spin-down time becomes zero in the dipole formula (so that quantitative results in some models such as the blitzar model can be affected). The corresponding spin-down time is given by

$$T_{\text{sd}} = \frac{3P_i^2 I c^3}{10\pi^2 B_*^2 R_*^6} \approx \begin{cases} 2.5 \text{ yr } B_{*,15}^{-2} P_{i,-0.5}^2 & (\text{magnetar}) \\ 2.5 \text{ yr } B_{*,12.5}^{-2} P_{i,-3}^2 & (\text{RNS}) \\ 2.9 \times 10^4 \text{ yr } B_{*,9}^{-2} P_{i,1}^2 & (\text{MWD}) \end{cases} \quad (3)$$

After $T > T_{\text{sd}}$, the rotation period increases as $P(T) \propto T^{1/2}$ and the spin-down power at the age T decreases as $L_{\text{sd}}(T) \propto T^{-2}$. In reality, the braking indices observed for Galactic pulsars differ from the theoretical value, but we use this formula for simplicity.

Next, we consider the baryonic ejecta outside the nebula. In the magnetar and RNS scenarios, we typically expect that the wind bubble is surrounded by the SN ejecta and we assume $M_{\text{ext}} \sim 3 M_\odot$ and $V_{\text{ext}} \sim 5000$ km s⁻¹, motivated by applications to luminous SNe including SLSNe (Kashiyama et al. 2016). Larger masses lead to more compact nebulae, where effects on the attenuation of non-thermal emission would become larger (Murase et al. 2015). In the MWD scenario, we assume that MWDs are formed by merger events, where the ejecta has $\sim 10^{-3} M_\odot$ and $V_{\text{ext}} \sim 10000$ km s⁻¹ (Ji et al. 2013). In this work, we denote the SN or merger ejecta as the “external” baryonic ejecta, which is expected to freely expand until the deceleration radius R_{ST} . This radius is expressed as

$$R_{\text{ST}} = \left(\frac{3M_{\text{ext}}}{4\pi n_{\text{ism}} m_p} \right)^{1/3} \approx \begin{cases} 9.6 \times 10^{18} \text{ cm } M_{\text{ext},0.5}^{1/3} n_{\text{ism}}^{-1/3} & (\text{SN}) \\ 6.6 \times 10^{17} \text{ cm } M_{\text{ext},-3}^{1/3} n_{\text{ism}}^{-1/3} & (\text{merger}) \end{cases} \quad (4)$$

The deceleration time is

$$T_{\text{ST}} \approx \begin{cases} 5.4 \times 10^2 \text{ yr } V_{\text{ext},8.75}^{-1} M_{\text{ext},0.5}^{1/3} n_{\text{ism}}^{-1/3} & (\text{magnetar}) \\ 1.2 \times 10^2 \text{ yr } P_{i,-3} M_{\text{ext},0.5}^{5/6} n_{\text{ism}}^{-1/3} & (\text{RNS}) \\ 21 \text{ yr } V_{\text{ext},9}^{-1} M_{\text{ext},-3}^{1/3} n_{\text{ism}}^{-1/3} & (\text{MWD}) \end{cases} \quad (5)$$

After the deceleration time, the nebula may be disrupted by the reverse shock (Blondin, Chevalier & Frierson 2001).

Thus, we consider very young nebulae with $T \lesssim 100 - 1000$ yr, although magnetic dissipation itself could happen in middle-age nebulae. The ejecta radius $R_{\text{ext}} \approx V_{\text{ext}}T$ is estimated to be

$$R_{\text{ext}} \simeq \begin{cases} 1.8 \times 10^{17} \text{ cm } V_{\text{ext},8.75} T_{10\text{yr}} & (\text{magnetar}) \\ 7.8 \times 10^{17} \text{ cm } P_{i,-3}^{-1} M_{\text{ext},0.5}^{-1/2} T_{10\text{yr}} & (\text{RNS}) \\ 3.2 \times 10^{17} \text{ cm } V_{\text{ext},9} T_{10\text{yr}} & (\text{MWD}) \end{cases} \quad (6)$$

Note that the external ejecta velocity V_{ext} is governed by the rotation energy if \mathcal{E}_{rot} exceeds the original explosion energy $\mathcal{E}_{\text{exp}} \sim 10^{51}$ erg, and the expression for $T > T_{\text{sd}}$ is shown here. The corresponding nucleon density is estimated to be

$$n_{\text{ext}} \simeq \begin{cases} 1.6 \times 10^5 \text{ cm}^{-3} M_{\text{ext},0.5} V_{\text{ext},8.75}^{-3} T_{10\text{yr}}^{-3} & (\text{magnetar}) \\ 1.9 \times 10^3 \text{ cm}^{-3} P_{i,-3}^3 M_{\text{ext},0.5}^{5/2} T_{10\text{yr}}^{-3} & (\text{RNS}) \\ 9.0 \text{ cm}^{-3} M_{\text{ext},-3} V_{\text{ext},9}^{-3} T_{10\text{yr}}^{-3} & (\text{MWD}) \end{cases} \quad (7)$$

Note that the free electron density would be significantly smaller since the ionization degree of the ejecta is expected to be low especially deep inside the ejecta. The typical SN ejecta becomes essentially neutral a few years after the SN explosion (Hamilton & Sarazin 1984). However, especially at early times, the column density of free electrons may reach $\sim 0.1 - 1000 \text{ pc cm}^{-3}$, which could contribute to the DM.

As noted above, the characteristic ejecta velocity is not affected by a central remnant for $\mathcal{E}_{\text{rot}} < \mathcal{E}_{\text{exp}}$. In this case, the nebular radius is given by (Chevalier 1977)

$$R_{\text{nb}} \approx \left(\frac{125 V_{\text{ext}}^3 L_{\text{sd},i}}{99 M_{\text{ext}}} \right)^{1/5} \begin{cases} T^{6/5} & (T < T_{\text{sd}}) \\ T_{\text{sd}}^{6/5} (T/T_{\text{sd}}) & (T > T_{\text{sd}}) \end{cases} \quad (8)$$

In the magnetar scenario, we have

$$R_{\text{nb}} \simeq \begin{cases} 2.5 \times 10^{15} \text{ cm } B_{*,15}^{2/5} P_{i,-0.5}^{-4/5} M_{\text{ext},0.5}^{-1/5} V_{\text{ext},8.75}^{3/5} T_{10\text{yr}}^{6/5} \\ 2.9 \times 10^{16} \text{ cm } P_{i,-0.5}^{-2/5} M_{\text{ext},0.5}^{-1/5} V_{\text{ext},8.75}^{3/5} T_{10\text{yr}} \end{cases} \quad (9)$$

whereas in the MWD scenario we have

$$R_{\text{nb}} \simeq 1.2 \times 10^{17} \text{ cm } B_{*,9}^{2/5} P_{i,1}^{-4/5} M_{\text{ext},-3}^{-1/5} V_{\text{ext},9}^{3/5} T_{10\text{yr}}^{6/5}. \quad (10)$$

When the rotation energy exceeds the original explosion energy, the ejecta dynamics is modified by the central remnant. Then, we have (Chevalier 2005)

$$R_{\text{nb}} \approx \left(\frac{8 L_{\text{sd},i}}{15 M_{\text{ext}}} \right)^{1/2} \begin{cases} T^{3/2} & (T < T_{\text{sd}}) \\ T_{\text{sd}}^{3/2} (T/T_{\text{sd}}) & (T > T_{\text{sd}}) \end{cases} \quad (11)$$

The nebular emission is assumed to come from a uniform sphere expanding at a constant velocity. This assumption is the easiest way to include the expansion of the nebula, although the realistic behavior of the expansion is more complicated. Then, we have

$$R_{\text{nb}} \simeq \begin{cases} 2.5 \times 10^{16} \text{ cm } B_{*,12.5} P_{i,-3}^{-2} M_{\text{ext},0.5}^{-1/2} T_{10\text{yr}}^{3/2} \\ 4.0 \times 10^{17} \text{ cm } P_{i,-3}^{-1} M_{\text{ext},0.5}^{-1/2} T_{10\text{yr}} \end{cases} \quad (12)$$

in the RNS scenario. We see that the nebular radius is expected to be $R_{\text{nb}} \sim 10^{16} - 10^{18}$ cm for $T \sim 10 - 100$ yr.

The nebular mass is uncertain, but a reasonable lower limit can be placed using the Goldreich-Julian density (Goldreich & Julian 1969). Using values at the co-rotation radius, the mass outflow rate at $T < T_{\text{sd}}$ is esti-

ated to be

$$\dot{M}_{\text{GJ}} \simeq \begin{cases} 2.5 \times 10^{-18} M_{\odot} \text{ s}^{-1} \mu_{\pm,6} B_{*,15} P_{i,0.5}^{-2} & (\text{magnetar}) \\ 7.9 \times 10^{-14} M_{\odot} \text{ s}^{-1} \mu_{\pm,6} B_{*,12.5} P_{i,-3}^{-2} & (\text{RNS}) \\ 3.1 \times 10^{-17} M_{\odot} \text{ s}^{-1} \mu_{\pm,6} B_{*,9} P_{i,1}^{-2} & (\text{MWD}) \end{cases} \quad (13)$$

where μ_{\pm} is the pair multiplicity (defined as the ratio of the pair density to the Goldreich-Julian density) and the wind is believed to be dominated by electron-positron pairs. Then, for $\mu_{\pm} \sim 10^5 - 10^6$, the mass accumulated during T would be

$$M_{\text{nb}} \gtrsim 10^{-9} - 10^{-5} M_{\odot}. \quad (14)$$

In this work, we use $M_{\text{nb}} \sim 10^{-7} M_{\odot}$ as a reference value, which is comparable to the ejecta mass suggested to explain afterglow emission following the 2004 giant flare of SGR 1806-20 (Gaensler et al. 2005; Granot et al. 2006). The nebular density is then estimated to be

$$n_{\text{nb}} \simeq 2.1 \times 10^3 \text{ cm}^{-3} M_{\text{nb},-7} P_{i,-0.5}^{6/5} M_{\text{ext},0.5}^{3/5} V_{\text{ext},8.75}^{-9/5} T_{10\text{yr}}^{-3} \quad (15)$$

in the magnetar scenario,

$$n_{\text{nb}} \simeq 8.0 \times 10^{-1} \text{ cm}^{-3} M_{\text{nb},-7} P_{i,-0.5}^3 M_{\text{ext},0.5}^{3/2} T_{10\text{yr}}^{-3} \quad (16)$$

in the RNS scenario, and

$$n_{\text{nb}} \simeq 1.7 \times 10^{-2} \text{ cm}^{-3} M_{\text{nb},-7} B_{*,9}^{-6/5} P_{i,1}^{12/5} \times M_{\text{ext},-3}^{3/5} V_{\text{ext},9}^{-9/5} T_{10\text{yr}}^{-18/5} \quad (17)$$

in the MWD scenario, respectively. Note that the column density may reach $n_{\text{nb}} R_{\text{nb}} \sim 0.001 - 100 \text{ pc cm}^{-3}$, which could contribute to the DM.

Note that the pair multiplicity is very uncertain and it is difficult to give a plausible theoretical value from first principles. As a result, its effect on the DM may be subject to a significant uncertainty, although results on the spectra are more insensitive (cf. Tanaka & Takahara 2013a). On the other hand, our calculations for HEGFs and their afterglows, which are shown in Section 3 and 4, are largely unaffected by this.

2.2 Quasi-steady nebular emission

Next, we model the emission of the nebula. Following Murase et al. (2015), we assume that the nebular emission mechanism and the parameters are similar to that for Galactic pulsar wind nebulae (e.g., Gaensler & Slane 2006; Tanaka & Takahara 2010, and references therein). For electrons and positrons, we consider a broken power-law injection spectrum,

$$\frac{d\dot{n}_e^{\text{nb}}}{d\gamma_e} \propto \begin{cases} \gamma_e^{-q_1} & (\gamma_m \leq \gamma_e \leq \gamma_b) \\ \gamma_e^{-q_2} & (\gamma_b < \gamma_e \leq \gamma_M) \end{cases} \quad (18)$$

where $q_1 \sim 1 - 1.5 (< 2)$ and $q_2 \sim 2.5 - 3 (> 2)$ are low- and high-energy spectral indices, and $\gamma_b \sim 10^4 - 10^6$ is the characteristic Lorentz factor of the accelerated leptons. A significant energy fraction ($\epsilon_e \sim 1$) of L_{sd} is used for non-thermal lepton acceleration (Rees & Gunn 1974; Kennel & Coroniti 1984; Tanaka & Takahara 2010, 2013b).

At sufficiently late times, the dominant radiation mechanism is the synchrotron process. The magnetic field energy

density in the nebula is parameterized as

$$U_B^{\text{nb}} = \epsilon_B \frac{3 \int dT L_{\text{sd}}}{4\pi R_{\text{nb}}^3}, \quad (19)$$

where $\epsilon_B \sim 0.001 - 0.01$ is the magnetic energy fraction, and we use $\epsilon_B = 0.01$ in this work. This value is based on results of detailed modeling of some of the known Galactic pulsar wind nebulae (Tanaka & Takahara 2010, 2013b). Although this assumption may not hold in early nebulae, it is reasonable and that our results in Sections 3 and 4 are not be much affected (see below).

In the magnetar scenario, the nebular magnetic field strength is estimated to be

$$B_{\text{nb}} \simeq 2.1 \times 10^{-2} \text{ G } P_{i,-0.5}^{-2/5} M_{\text{ext},0.5}^{3/10} V_{\text{ext},8.75}^{-9/10} T_{10\text{yr}}^{-3/2} \epsilon_{B,-2}^{1/2} \quad (20)$$

for $T > T_{\text{sd}}$. Similarly, we have

$$B_{\text{nb}} \simeq 1.3 \times 10^{-1} \text{ G } P_{i,-3}^{1/2} M_{\text{ext},0.5}^{3/4} T_{10\text{yr}}^{-3/2} \epsilon_{B,-2}^{1/2} \quad (21)$$

in the RNS scenario and

$$B_{\text{nb}} \simeq 6.5 \times 10^{-4} \text{ G } B_{*,9}^{2/5} P_{i,1}^{-4/5} M_{\text{ext},-3}^{3/10} V_{\text{ext},9}^{-9/10} T_{10\text{yr}}^{-13/10} \epsilon_{B,-2}^{1/2} \quad (22)$$

in the MWD scenario, respectively.

Taking the magnetar scenario as an example, the characteristic synchrotron frequency of the nebular emission is

$$\begin{aligned} \nu_b &\approx \frac{3}{4\pi} \gamma_b^2 \frac{e B_{\text{nb}}}{m_e c} \\ &\simeq 9.0 \times 10^{14} \text{ Hz } \gamma_{b,5}^2 P_{i,-0.5}^{-2/5} R_{*,6}^{2/5} \epsilon_{B,-2}^{1/2} \\ &\times M_{\text{ext},0.5}^{3/10} V_{\text{ext},8.5}^{-9/10} T_{10\text{yr}}^{-3/2}. \end{aligned} \quad (23)$$

The cooling Lorentz factor of electrons is determined by $t_{\text{syn}} = T$, which is

$$\begin{aligned} \gamma_c &\approx \frac{6\pi m_e c}{\sigma_T B_{\text{nb}}^2 T} \\ &\simeq 5300 P_{i,-0.5}^{4/5} R_{*,6}^{-4/5} M_{\text{ext},0.5}^{-3/5} V_{\text{ext},8.5}^{9/5} T_{10\text{yr}}^2 \epsilon_{B,-2}^{-1}, \end{aligned} \quad (24)$$

and the corresponding cooling synchrotron frequency is

$$\begin{aligned} \nu_c &\approx \frac{3}{4\pi} \gamma_c^2 \frac{e B_{\text{nb}}}{m_e c} \\ &\simeq 2.6 \times 10^{12} \text{ Hz } P_{i,-0.5}^{6/5} R_{*,6}^{-6/5} \epsilon_{B,-2}^{-3/2} \\ &\times M_{\text{ext},0.5}^{-9/10} V_{\text{ext},8.5}^{27/10} T_{10\text{yr}}^{5/2}. \end{aligned} \quad (25)$$

Note that the maximum synchrotron frequency is

$$\nu_M \approx \frac{9}{4} \frac{m_e c^3}{2\pi e^2} \simeq 3.8 \times 10^{22} \text{ Hz}, \quad (26)$$

which does not depend on ϵ_B . This is obtained simply by equating half of the Larmor time with the synchrotron cooling time (e.g., Bühler & Blandford 2014; Komissarov & Lyutikov 2011; Kohri, Ohira & Ioka 2012).

In the fast-cooling case ($\nu_c < \nu_b$), the synchrotron spectrum is expressed as

$$\nu L_\nu^{\text{nb}} \sim \frac{\epsilon_e L_{\text{sd}}}{2\mathcal{R}_b} \begin{cases} (\nu/\nu_b)^{(2-q_1)/2} & (\nu_c \leq \nu \leq \nu_b) \\ (\nu/\nu_b)^{(2-q_2)/2} & (\nu_b < \nu \leq \nu_M) \end{cases} \quad (27)$$

where $\mathcal{R}_b \sim (2 - q_1)^{-1} + (q_2 - 2)^{-1} \sim 5$. The slow-cooling

synchrotron spectrum ($\nu_b < \nu_c$) is written as

$$\nu L_\nu^{\text{nb}} \sim \frac{\epsilon_e L_{\text{sd}}}{2\mathcal{R}_b} \begin{cases} (\nu_b/\nu_c)^{(3-q_2)/2} (\nu/\nu_b)^{(3-q_1)/2} & (\nu \leq \nu_b) \\ (\nu/\nu_c)^{(3-q_2)/2} & (\nu_b \leq \nu \leq \nu_c) \\ (\nu/\nu_c)^{(2-q_2)/2} & (\nu_c < \nu \leq \nu_M) \end{cases} \quad (28)$$

We numerically calculate the spectra of the nebular emission following the method used in Murase et al. (2015). We include the synchrotron and inverse-Compton emission processes, and solve the time-dependent kinetic equations taking into account electromagnetic cascades. The cosmic microwave background and extragalactic background light are included as external radiation fields. Note that the SN or merger emission is important at early times from weeks to months (Murase et al. 2015; Kotera, Phinney & Olinto 2013), but such a very early phase is beyond the scope of this work. The synchrotron self-absorption (SSA) process and the Razin effect are also taken into account in the calculations. The numerical results are shown in Fig. 2. See the Appendix for more details on light curves and a discussion on the detectability of emission from quasi-steady nebulae.

Note that the nebular emission is relevant even if it is itself undetectable. As we discuss in the next subsection, it can prevent high-energy gamma-rays and radio waves from escaping the nebula.

2.3 Gamma-ray and radio attenuation in the nebula and ejecta

Based on the nebula model described above, we consider the fate of the radio and gamma-ray emission. As discussed in Section 3, HEGFs and/or FRBs may be generated inside the nebula, and it is natural to ask whether these emissions can escape or not from the nebula. Our numerical results for various absorption processes in the three scenarios with nominal parameters are shown in Fig. 3 as a function of the age T . Here the calculations are performed based on the spectral energy distributions shown in Figs. 2.

For gamma-rays, we consider the two-photon annihilation process ($\gamma\gamma \rightarrow e^-e^+$) in the nebula and the Bethe-Heitler process ($\gamma A \rightarrow e^-e^+A$) in the external ejecta. The optical depth to two-photon annihilation is calculated by

$$\tau_{\gamma\gamma}^{\text{nb}}(\epsilon_\gamma) = R_{\text{nb}} \int d\nu n_\nu^{\text{nb}} \int \frac{d\cos\theta}{2} (1 - \cos\theta) \sigma_{\gamma\gamma}(\epsilon_\gamma, \cos\theta), \quad (29)$$

where n_ν^{nb} is the photon density in the nebula and θ is the angle between two photons. As shown in Fig. 3, we find that the gamma-ray escape of TeV photons is possible in all three scenarios³. However, because of the large spin-down power, the escape is prevented until $T \sim 10$ yr in the RNS scenario (see the middle panel of Fig. 3). The Bethe-Heitler pair-production process is calculated following Murase et al. (2015), and the resulting attenuation turns out to be more negligible even in the RNS and MWD scenarios.

The escape of radio waves including FRB emission is

³ Note that, as studied in Murase et al. (2015), the SN emission is relevant in embryonic nebulae ($T \lesssim 1$ yr) and gamma-ray escape can be prevented by the two-photon annihilation process.

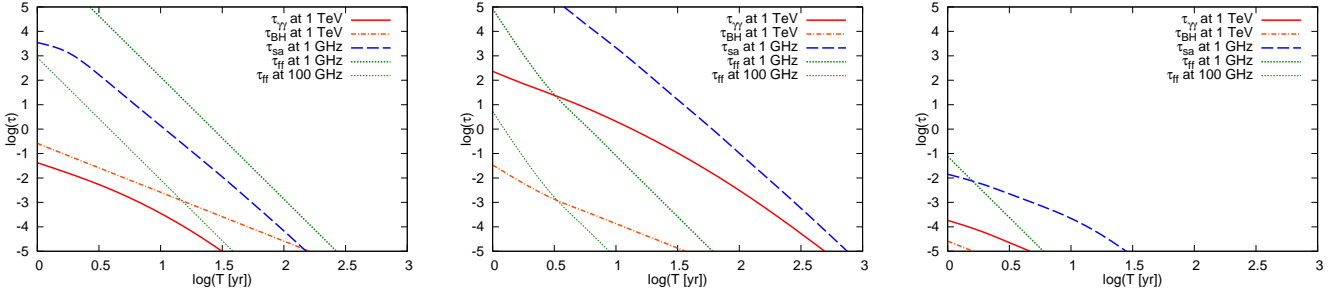


Figure 3. Optical depths to the two-photon annihilation, Bethe-Heitler pair-production, SSA, and free-free absorption processes as a function of the age T , considering 1 TeV gamma-rays and radio waves at 1 GHz and 100 GHz as examples. Corresponding to Fig. 2, the values for the magnetar scenario (left panel), RNS scenario (middle panel), and MWD scenario (right panel) are shown.

more difficult. One of the relevant processes is the SSA process in the nebula (e.g., Yang, Zhang & Dai 2016). The SSA optical depth is calculated as

$$\tau_{\text{sa}}^{\text{nb}}(\nu) = R_{\text{nb}} \int d\gamma_e \frac{dn_e^{\text{nb}}}{d\gamma_e} \sigma_{\text{sa}}(\nu, \gamma_e), \quad (30)$$

where the SSA cross section is (e.g., Ghisellini & Svensson 1991)

$$\sigma_{\text{sa}}(\nu, \gamma_e) = \frac{1}{2m_e\nu^2\gamma_e p_e} \frac{\partial}{\partial\gamma_e} [\gamma_e p_e j_{\text{syn}}(\nu, \gamma_e)], \quad (31)$$

where j_{syn} is the synchrotron emissivity and p_e is the electron momentum. The relevance of the SSA is already seen in Fig. 2, where an SSA cutoff appears at $\gtrsim 1$ GHz at early times. The evolution of the SSA optical depth is shown in Fig. 3. In the magnetar scenario, the nebula is opaque against radio waves until $T \sim 5$ yr, while in the RNS scenario, the GHz radio emission can get out only at times $T \gtrsim 30$ yr. However, as shown in Figs. 2 and 3, the escape of higher-frequency radio waves, e.g., at 100 GHz, is more readily possible.

The free-free absorption in the external ejecta can be relevant, although it depends on the amount of free electrons, which is uncertain. In Fig. 3, assuming a mean atomic number $\bar{A} = 10$, $\bar{Z} = 5$, and the singly ionized state⁴ (implying the electron density $n_e^{\text{ext}} \approx n_{\text{ext}} \hat{\mu}_e^{-1} \sim n_{\text{ext}}/\bar{A}$) with $T_{\text{ext}} = 10^4$ K (Hamilton & Sarazin 1984), we estimate the free-free absorption optical depth (τ_{ff}). Note that realistic values may be smaller since the external ejecta is expected to be essentially neutral at late times. As shown in Fig. 3, the free-free absorption can be the most relevant for the propagation of radio waves in the magnetar scenario, and the radio waves may be absorbed at $T \lesssim 30 - 100$ yr. In the RNS scenario, due to the large spin-down power, the SSA process is expected to play a dominant role in the attenuation of radio waves. In the MWD scenario, the system is transparent to both radio and gamma-ray emission.

We also calculate the DM due to the baryonic ejecta, and the results are shown in Fig. 4. In principle, it is possible for the baryonic ejecta to significantly contribute to the DM.

⁴ In the earlier version of this paper, for the calculation of free-free absorption, the fully ionized state with $T_{\text{ext}} = 10^{2.5}$ K was actually assumed. Here more realistic parameters are used.

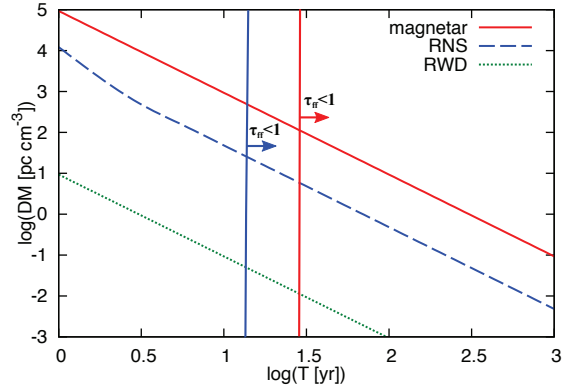


Figure 4. Time evolution of the local DM due to the baryonic ejecta, for three scenarios considered in this work.

However, interestingly, we find that the ejecta contribution may typically be limited to $\text{DM} \lesssim 10 - 100 \text{ pc cm}^{-3}$, because large densities of ionized electrons also increase τ_{ff} .

There are other plasma processes that could also be relevant. The plasma frequency is given by $\nu_{\text{pl}} = (1/2\pi) \times (4\pi n_e^{\text{ext}} e^2 / m_e)^{1/2} \simeq 9.0 \times 10^5 \text{ Hz} \sqrt{n_{e,4}^{\text{ext}}}$, below which electromagnetic waves cannot propagate in the medium. One can see that the induced-Compton and induced-Raman scattering in the cold plasma can be neglected at $T \gtrsim 30 - 100$ yr. For example, the optical depth to the induced-Compton scattering in the external ejecta is estimated to be (e.g., Wilson & Rees 1978; Lyubarsky 2008)

$$\begin{aligned} \tau_{\text{ind}}^{\text{ext}}(\nu) &\approx \frac{3\sigma_T c n_e^{\text{ext}} L_{\text{FRB}} \Delta t}{32\pi^2 m_e \nu^3 R_{\text{ext}}^2} \\ &\simeq 2.1 \times 10^{-6} L_{\text{FRB},43} \Delta t_{-3} \nu_9^{-3} n_{e,4}^{\text{ext}} R_{\text{ext},17}^{-2}. \end{aligned} \quad (32)$$

3 HIGH-ENERGY GAMMA-RAY FLASHES

Pulsar winds are highly relativistic outflows that are initially Poynting-dominated (Michel 1969). An impulsive energy injection with an intrinsic duration δt , which may originate from magnetic dissipation in the magnetosphere (e.g.,

Thompson & Duncan 1995, 2001) or around current sheets in the wind zone (e.g., Gill & Heyl 2010; Elenbaas et al. 2016), or perhaps from the spin-down power, may lead to the formation of a highly relativistic outflow with Lorentz factors Γ_0 . Such a highly relativistic impulse is expected to initially propagate in the pre-existing pulsar wind, which is itself also Poynting-dominated. We focus on cases of $\Gamma_0 \gg 1$, although the bulk acceleration depends on how many pairs are loaded in the flow as well as details of the magnetic dissipation⁵. The magnetic energy would be the most promising energy source in our model. The magnetic energy tapped in the star is (cf. Katz 1982; Kashiyama, Ioka & Mészáros 2013; Zhang 2014)

$$\begin{aligned} \mathcal{E}_{\text{mag}} &\approx \frac{1}{6} B_*^2 R_*^3 \\ &= \begin{cases} 1.7 \times 10^{48} \text{ erg } B_{c,15.5}^2 R_{*,6}^3 & \text{(magnetar)} \\ 1.7 \times 10^{43} \text{ erg } B_{c,13}^2 R_{*,6}^3 & \text{(RNS)} \\ 2.1 \times 10^{45} \text{ erg } B_{c,9.5}^2 R_{*,8.7}^3 & \text{(MWD)} \end{cases} \quad (33) \end{aligned}$$

where B_c is the internal magnetic field, which could be larger than the surface magnetic field B_* . Note also that, in principle, the spin-down power L_{sd} can be relevant as an alternative energy source in a certain model involving RNSs (e.g., Totani 2013, for NS-NS mergers).

Hereafter, we use t as the elapsed time after a burst. The distance between a compact remnant and its nebula is denoted by r_0 , which can be smaller than R_{nb} . Note that the central remnant may receive a kick by, e.g., the SN explosion. In the NS case, the typical kick velocity is $V_k \sim 500 \text{ km s}^{-1}$. The distance the NS travels is $R_k \approx V_k T \simeq 1.6 \times 10^{17} \text{ cm } (V_k/500 \text{ km s}^{-1}) T_{10\text{yr}}$, which can be comparable to R_{nb} , and r_0 is given by $r_0 = R_{\text{nb}} - R_k$ for $R_k < R_{\text{nb}}$.

3.1 GeV-TeV flashes from a forward shock

An impulsive flow with $\Gamma_0 \sim 10^4 - 10^6$ is decelerated as soon as it reaches the nebula. The deceleration is quick since the deceleration radius $r_\Gamma \approx [3\mathcal{E}/(4\pi n_{\text{nb}} m_e c^2 \Gamma_0^2)]^{1/3}$ is typically much smaller than r_0 . For a sufficiently large energy injected into the nebula, the compressed nebula becomes relativistic. As suggested for the Crab pulsar flares (e.g., Bühler & Blandford 2014; Komissarov & Lyutikov 2011; Kohri, Ohira & Ioka 2012), the Doppler-boosted nebular emission may generate photons whose energy is higher than the synchrotron energy limited by radiation losses, and a possible application to FRBs has also been discussed (Lyubarsky 2014). We assume that the shell width at r_0 is $c\Delta t$ in the observer frame, where $\Delta t \approx \max[\delta t, r_0/(2\Gamma_0^2 c)]$ gives the duration of the HEGFs. The duration can be $\Delta t \approx \delta t \sim 1 \text{ ms}$ (as in FRBs), but it may be as long as $\Delta t \approx r_0/(2\Gamma_0^2 c) \simeq 1700 \text{ s } r_{0,16} \Gamma_{0,1}^{-2}$ (for GRB-flare-like Lorentz factors). The Lorentz factor of the shocked region Γ can be determined by the pressure balance. For a magnetic piston or unmagnetized ejecta in the thick shell limit, Γ is estimated by $\mathcal{E}/(4\pi r^2 \Gamma^2 c \Delta t) \approx 4\Gamma^2 p_{\text{nb}} \xi$, where p_{nb} is

the nebular pressure and $\xi < 1$ is a pre-factor due to radiation energy losses. The Lorentz factor of the shocked region roughly becomes

$$\Gamma \sim \begin{cases} 1100 \mathcal{E}_{48}^{1/4} B_{*,15}^{1/2} \Delta t_{-3}^{-1/4} T_{10\text{yr}}^{1/2} & \text{(magnetar)} \\ 3.6 \mathcal{E}_{43}^{1/4} B_{*,12.5}^{1/2} \Delta t_{-3}^{-1/4} T_{10\text{yr}}^{1/2} & \text{(RNS)} \\ 280 \mathcal{E}_{45}^{1/4} B_{*,9}^{-1/2} P_{i,1} \Delta t_{-3}^{-1/4} & \text{(MWD)} \end{cases} \quad (34)$$

in the three scenarios. Hereafter, we consider $\Gamma \sim 10 - 1000$, and in this subsection, for demonstration purposes, we use the reference parameters of the magnetar scenario.

In young nebulae, the immediate upstream is filled with pre-accelerated particles with a typical Lorentz factor of γ_b (for the original nebula). If there is no cooling and the shell is thick enough for particles to be thermalized, the injection Lorentz factor (in the rest frame of the flow moving with Γ) is given by

$$\gamma'_i \approx \Gamma \gamma_b = 10^8 \Gamma_3 \gamma_{b,5}, \quad (35)$$

and the corresponding synchrotron energy is given by

$$\begin{aligned} \varepsilon_i &\approx \frac{3}{4\pi} \Gamma \hbar \gamma_i'^2 \frac{eB'}{m_e c} \\ &\simeq 3.7 \text{ TeV } \Gamma_3^4 \gamma_{b,5}^2 P_{i,-0.5}^{-2/5} R_{*,6}^{2/5} M_{\text{ext},0.5}^{3/10} V_{\text{ext},8.75}^{-9/10} T_{10\text{yr}}^{-3/2}. \end{aligned} \quad (36)$$

As a conservative choice, we adopt the shock-compressed field value $B' \approx \Gamma B_{\text{nb}}$ for the evaluation of synchrotron emission from the shocked nebula. The synchrotron cooling Lorentz factor (for the refreshed nebula) is given by

$$\gamma'_c \approx 8.4 \times 10^5 \Gamma_3^{-3} P_{i,-0.5}^{4/5} R_{*,6}^{-4/5} M_{\text{ext},0.5}^{-3/5} V_{\text{ext},8.75}^{9/5} T_{10\text{yr}}^3 \Delta t_{-3}^{-1}, \quad (37)$$

and the corresponding synchrotron cooling energy is

$$\varepsilon_c \simeq 0.26 \text{ GeV } \Gamma_3^{-4} P_{i,-0.5}^{6/5} R_{*,6}^{-6/5} M_{\text{ext},0.5}^{-9/10} V_{\text{ext},8.75}^{27/10} T_{10\text{yr}}^{9/2} \Delta t_{-3}^{-2}. \quad (38)$$

Note that the Lorentz factor of accelerated leptons is limited by $r'_L/(2c) = 6\pi m_e c/(\gamma' \sigma_T B'^2)$ and $r'_L/(2c) = l'/c \approx \Gamma \Delta t$. The former condition gives

$$\begin{aligned} \gamma'_{M1} &\approx \left(\frac{3m_e^2 c^4}{2B'e^3} \right)^{1/2} \simeq 2.1 \times 10^7 \Gamma_3^{-1/2} P_{i,-0.5}^{1/5} R_{*,6}^{-1/5} \epsilon_{B,-2}^{-1/4} \\ &\quad \times M_{\text{ext},0.5}^{-3/20} V_{\text{ext},8.75}^{9/20} T_{10\text{yr}}^{3/4}, \end{aligned} \quad (39)$$

and the latter condition gives

$$\begin{aligned} \gamma'_{M2} &\approx \left(\frac{2eB'l'}{m_e c^2} \right) \simeq 7.5 \times 10^8 \Gamma_3^2 P_{i,-0.5}^{-2/5} R_{*,6}^{2/5} \epsilon_{B,-2}^{1/2} \\ &\quad \times M_{\text{ext},0.5}^{3/10} V_{\text{ext},8.75}^{-9/10} T_{10\text{yr}}^{-3/2} \Delta t_{-3}. \end{aligned} \quad (40)$$

The corresponding maximum synchrotron energies are

$$\varepsilon_{M1} \simeq 0.15 \text{ TeV } \Gamma_3 \quad (41)$$

and

$$\begin{aligned} \varepsilon_{M2} &\simeq 2.1 \times 10^2 \text{ TeV } \Gamma_3^6 P_{i,-0.5}^{-6/5} R_{*,6}^{6/5} \epsilon_{B,-2}^{3/2} \\ &\quad \times M_{\text{ext},0.5}^{9/10} V_{\text{ext},8.75}^{-27/10} T_{10\text{yr}}^{-9/2} \Delta t_{-3}^2, \end{aligned} \quad (42)$$

and the maximum synchrotron energy is $\varepsilon_M = \min[\varepsilon_{M1}, \varepsilon_{M2}]$. Note that ε_{M1} does not depend on ϵ_B explicitly, so predictions for HEGFs may not be very sensitive to the magnetic fields in the nebula.

⁵ There may be prompt emission associated with magnetic reconnections. In the magnetar scenario, it may be observed as giant flares (or short bursts in X-rays), as discussed in Section 5.

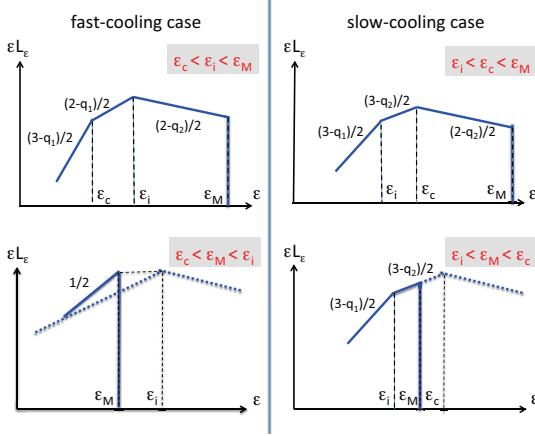


Figure 5. Typical synchrotron spectra of HEGF emission. The typical energy is expected to be at GeV-TeV energies for the forward shock emission.

In the conventional fast-cooling case ($\varepsilon_c < \varepsilon_i < \varepsilon_M$), the synchrotron spectrum is given by

$$\varepsilon L_\varepsilon^{\text{FS}} \propto \begin{cases} (\varepsilon_c/\varepsilon_i)^{(2-q_1)/2} (\varepsilon/\varepsilon_c)^{(3-q_1)/2} & (\varepsilon < \varepsilon_c) \\ (\varepsilon/\varepsilon_i)^{(2-q_1)/2} & (\varepsilon_c \leq \varepsilon \leq \varepsilon_i) \\ (\varepsilon/\varepsilon_i)^{(2-q_2)/2} & (\varepsilon_i < \varepsilon \leq \varepsilon_M) \end{cases} \quad (43)$$

However, for $\varepsilon_c < \varepsilon_M < \varepsilon_i$, most of the energy is released before the electrons and positrons are boosted to γ'_i . In this situation, one expects that the lepton distribution would pile up around γ'_M , leading to a spectral bump around ε_M .

$$\varepsilon L_\varepsilon^{\text{FS}} \propto (\varepsilon/\varepsilon_M)^{1/2} \quad (\varepsilon \lesssim \varepsilon_M) \quad (44)$$

The schematic picture is shown in Fig. 5. In the fast-cooling case, the radiation energy per logarithmic energy is

$$(\varepsilon_M L_{\varepsilon_M}^{\text{FS}}) \Delta t \sim (\mathcal{E}/2\mathcal{R}_b) \sim 10^{47} \text{ erg } \mathcal{E}_{48}. \quad (45)$$

In the magnetar scenario, one can expect to be in the fast-cooling case for $T \lesssim 300$ yr (see below). Then, the TeV gamma-ray fluence from a HEGF is $\varepsilon^2 \phi_\gamma \sim 8 \times 10^{-7} \text{ erg cm}^{-2} \mathcal{E}_{48} d_{26}^{-2}$. On the other hand, the Fermi-LAT 5σ sensitivity at ~ 100 GeV is $\sim 10^{-4} \text{ erg cm}^{-2}$, which is insufficient to detect such HEGFs. For this one would need larger gamma-ray detectors, such as the High-Altitude Water Cherenkov Observatory (HAWC), which has an effective area of $\sim 100 \text{ m}^2$ at 100 GeV and $2 \times 10^4 \text{ m}^2$ at 1 TeV, respectively (Abeysekara et al. 2013). The fluence sensitivity in the 0.1–1 TeV range is $\sim \text{a few } \times 10^{-7} \text{ erg cm}^{-2}$, so HAWC may be able to detect a nearby HEGF within $\sim 10\text{--}100$ Mpc if $\mathcal{E} \sim 10^{46}\text{--}10^{48}$ erg. If the HEGF rate is $R_{\text{HEGF}} \sim 10^4 \text{ Gpc}^{-3} \text{ yr}^{-1}$, the event rate is $\sim 0.02\text{--}20 R_{\text{HEGF},4} \text{ yr}^{-1}$. The future Cherenkov Telescope Array (CTA) is expected to have an effective area of $\sim 10^6 \text{ m}^2$ at 1 TeV. The corresponding fluence sensitivity would be $\sim 10^{-9} \text{ erg cm}^{-2}$, implying that the detection horizon of HEGFs is $\sim 0.1\text{--}1$ Gpc. The CTA's Medium Size Telescopes of 12 m and 9.66 m will have a field of view of 8° , so the event rate in CTA's field of view may be $\sim 0.006\text{--}6 R_{\text{HEGF},4} \text{ yr}^{-1}$ with a duty cycle of

10 percent⁶. On the other hand, in the slow cooling regime, only a fraction of the particle energy is released as radiation, which is typically the case in the RNS and MWD scenarios. For $\varepsilon_i < \varepsilon_c < \varepsilon_M$, we have the conventional slow-cooling spectrum, which is

$$\varepsilon L_\varepsilon^{\text{FS}} \propto \begin{cases} (\varepsilon_i/\varepsilon_c)^{(3-q_2)/2} (\varepsilon/\varepsilon_i)^{(3-q_1)/2} & (\varepsilon < \varepsilon_i) \\ (\varepsilon/\varepsilon_c)^{(3-q_2)/2} & (\varepsilon_i \leq \varepsilon \leq \varepsilon_c) \\ (\varepsilon/\varepsilon_c)^{(2-q_2)/2} & (\varepsilon_c < \varepsilon \leq \varepsilon_M) \end{cases} \quad (46)$$

where the radiation energy is limited by

$$(\varepsilon_M L_{\varepsilon_M}^{\text{FS}}) \Delta t \sim (\mathcal{E}/2\mathcal{R}_b) (\varepsilon_c/\varepsilon_i)^{(2-q_2)/2}. \quad (47)$$

For $\varepsilon_i < \varepsilon_M < \varepsilon_c$, we obtain

$$\varepsilon L_\varepsilon^{\text{FS}} \propto \begin{cases} (\varepsilon_i/\varepsilon_c)^{(3-q_2)/2} (\varepsilon/\varepsilon_i)^{(3-q_1)/2} & (\varepsilon < \varepsilon_i) \\ (\varepsilon/\varepsilon_c)^{(3-q_2)/2} & (\varepsilon_i \leq \varepsilon \leq \varepsilon_M) \end{cases} \quad (48)$$

and

$$(\varepsilon_M L_{\varepsilon_M}^{\text{FS}}) \Delta t \sim (\mathcal{E}/2\mathcal{R}_b) (\varepsilon_c/\varepsilon_i)^{(2-q_2)/2} (\varepsilon_M/\varepsilon_c)^{(3-q_2)/2}. \quad (49)$$

In any case, the radiation energy is smaller than in the fast-cooling case, so it would be more difficult to be detected through HEGFs. Note that we do not consider cases of $\varepsilon_M < \varepsilon_i, \varepsilon_c$, where upstream particles with γ'_i would be advected before they are thermalized or cooled by radiation. The radiation would be very inefficient and the properties of such shocks are less clear.

A natural question concerns the conditions for the fast-cooling regime to be realized. The critical Lorentz factor such that $\varepsilon_i = \varepsilon_c$ is given by

$$\begin{aligned} \Gamma_{\text{cri}} &\approx 300 \gamma_{b,5}^{-1/4} P_{i,-0.5}^{1/5} \epsilon_{B,-2}^{-1/4} \\ &\times M_{\text{ext},0.5}^{-3/20} V_{\text{ext},8.75}^{9/20} T_{10\text{yr}}^{3/4} \Delta t_{-3}^{-1/4} \end{aligned} \quad (50)$$

in the magnetar scenario. Similarly, we have

$$\begin{aligned} \Gamma_{\text{cri}} &\approx 120 \gamma_{b,5}^{-1/4} P_{i,-3}^{-1/4} \epsilon_{B,-2}^{-1/4} \\ &\times M_{\text{ext},0.5}^{-3/8} T_{10\text{yr}}^{3/4} \Delta t_{-3}^{-1/4} \end{aligned} \quad (51)$$

in the RNS scenario and

$$\begin{aligned} \Gamma_{\text{cri}} &\approx 1700 \gamma_{b,5}^{-1/4} B_{*,9}^{-1/5} P_{i,1}^{2/5} \epsilon_{B,-2}^{-1/4} \\ &\times M_{\text{ext},-3}^{-3/20} V_{\text{ext},9}^{9/20} T_{10\text{yr}}^{13/20} \Delta t_{-3}^{-1/4} \end{aligned} \quad (52)$$

in the MWD scenario. The critical Lorentz factor at which $\varepsilon_M = \varepsilon_c$ is given by

$$\begin{aligned} \Gamma_{\text{crM}} &\approx 280 P_{i,-0.5}^{6/25} \epsilon_{B,-2}^{-3/10} \\ &\times M_{\text{ext},0.5}^{-9/50} V_{\text{ext},8.75}^{27/50} T_{10\text{yr}}^{9/10} \Delta t_{-3}^{-2/5} \end{aligned} \quad (53)$$

in the magnetar scenario. Similarly, we have

$$\begin{aligned} \Gamma_{\text{crM}} &\approx 93 P_{i,-3}^{-3/10} \epsilon_{B,-2}^{-3/10} \\ &\times M_{\text{ext},0.5}^{-9/20} T_{10\text{yr}}^{9/10} \Delta t_{-3}^{-2/5} \end{aligned} \quad (54)$$

⁶ For more detailed estimates of the event rate, see Kakuwa et al. (2012) that considers the detectability of GRBs at very high-energies.

in the RNS scenario and

$$\begin{aligned} \Gamma_{\text{crM}} &\approx 2300 B_{*,9}^{-6/25} P_{i,1}^{12/25} \epsilon_{B,-2}^{-3/10} \\ &\times M_{\text{ext},-3}^{-9/50} V_{\text{ext},9}^{27/50} T_{10\text{yr}}^{39/50} \Delta t_{-3}^{-2/5} \end{aligned} \quad (55)$$

in the MWD scenario. These imply that the slow-cooling spectrum is typically expected in the RNS and MWD scenarios, and the radiation efficiency of HEGFs is not much larger. In the magnetar scenario, the efficient TeV emission is possible for $T \lesssim 300$ yr. Hence, if a magnetic burst can occur during the lifetime (which is $\sim 10^3 - 10^4$ yr in the magnetar scenario), we expect that strong HEGFs accompany a fraction of the bursts that occur in wind bubbles.

3.2 MeV-GeV flashes from a reverse shock

It is thought that the classical shock acceleration mechanism is inefficient for highly magnetized shocks (e.g., Sironi & Spitkovsky 2009), so the non-thermal emission from the shocked wind would depend on the magnetization parameter of the impulsive flow (σ_0 at r_0). Here we discuss possible particle acceleration at the reverse shock which may occur especially if $\sigma_0 \lesssim 1$ or in the presence of magnetic reconnection. We use the magnetar scenario as an example.

Assuming a flow with $\Gamma_0 \gg 1$, the relative Lorentz factor is estimated to be

$$\Gamma_{\text{rel}} \approx \frac{\Gamma_0}{2\Gamma} = 500 \Gamma_{0,6} \Gamma_3^{-1}. \quad (56)$$

As in the ordinary nebula case, we assume $\gamma'_b \approx \Gamma_{\text{rel}}$. Then, the characteristic synchrotron energy in the observer frame becomes

$$\begin{aligned} \epsilon_b &\simeq 40 \text{ eV } \Gamma_3^{-2} \Gamma_{0,6}^2 \mathcal{E}_{48}^{1/2} P_{i,-0.5}^{2/5} R_{*,6}^{-6/5} \\ &\times M_{\text{ext},0.5}^{1/5} V_{\text{ext},8.75}^{-3/5} \epsilon_B^{1/2} T_{10\text{yr}}^{-1} \Delta t_{-3}^{-1/2}. \end{aligned} \quad (57)$$

On the other hand, the synchrotron cooling Lorentz factor (for the shocked wind) is given by

$$\gamma'_c \approx 5.0 \times 10^6 \Gamma_3 \mathcal{E}_{48}^{-1} P_{i,-0.5}^{-4/5} R_{*,6}^{4/5} \epsilon_B^{-1} M_{\text{ext},0.5}^{-2/5} V_{\text{ext},8.75}^{6/5} T_{10\text{yr}}^2, \quad (58)$$

and the corresponding synchrotron cooling energy is

$$\begin{aligned} \epsilon_c &\simeq 3.8 \text{ GeV } \Gamma_3^2 \mathcal{E}_{48}^{-3/2} P_{i,-0.5}^{-6/5} R_{*,6}^{6/5} \epsilon_B^{-3/2} \\ &\times M_{\text{ext},0.5}^{-3/5} V_{\text{ext},8.75}^{9/5} T_{10\text{yr}}^3 \Delta t_{-3}^{-1/2}. \end{aligned} \quad (59)$$

The maximum synchrotron energy is

$$\epsilon_M \simeq 0.15 \text{ TeV } \Gamma_3. \quad (60)$$

The synchrotron spectrum is expected to be in the slow-cooling regime. As in Eq. (47), the released energy is limited by

$$\begin{aligned} \mathcal{E}_{\text{RS}} &\sim 3 \times 10^{46} \text{ erg } \mathcal{E}_{48}^{q_2-1} \Gamma_3^{4-2q_2} \Gamma_{0,6}^{q_2-2} \epsilon_B^{q_2-2} f_e P_{i,-0.5}^{4q_2/5-8/5} \\ &\times R_{*,6}^{8/5-4q_2/5} M_{\text{ext},0.5}^{2q_2/5-4/5} V_{\text{ext},8.75}^{12/5-6q_2/5} T_{10\text{yr}}^{4-2q_2}. \end{aligned} \quad (61)$$

Thus, we expect that the forward shock emission is typically more relevant for the purpose of detecting flaring nebular emission. Note that the characteristic frequencies are sensitive to Γ_{rel} , and smaller values lead to lower-energy gamma-ray emission that could be in the MeV range.

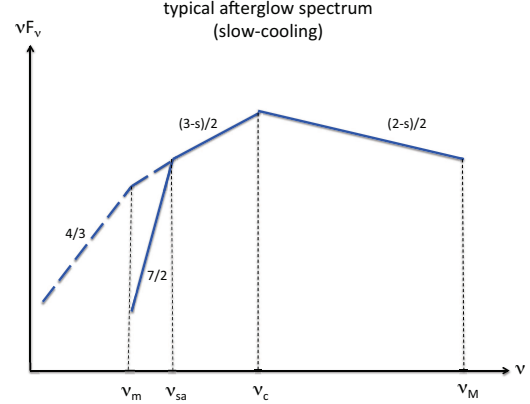


Figure 6. A typical synchrotron spectrum of afterglow emission that follows a HEGF and FRB.

4 BROADBAND AFTERGLOW EMISSION

In the previous section, we considered a burst with an explosion energy $\mathcal{E} \sim 10^{43} - 10^{48}$ erg. An energetic relativistic outflow triggered by the burst would sweep the nebula after it crosses the termination shock. Then, as the nebula is hot, the shock will disappear as the shocked flow becomes sub-sonic. The shell merges into the nebula, and would start expanding $\sqrt{3}r_0/c \simeq 10^6$ s $r_{0,16}$ after the burst. Here we consider the refreshed forward shock formed as it interacts with the external baryonic ejecta. We assume that the plasma in the shock vicinity is fully ionized by the external shock.

To discuss the detectability, we use fiducial values of the magnetar scenario. However, the setup is generic and can be applied to giant flares of soft gamma-ray repeaters and merger scenarios. In the giant flare case, our model is actually analogous to its afterglow model (Gaensler et al. 2005). In the merger case, a possible application could be considered if a long-lived magnetar exists.

In the inelastic collision limit, assuming momentum and energy conservation, the merged shell (which we call the inner ejecta) has a Lorentz factor of

$$\Gamma_{\text{ej}} \approx \frac{1 + \mathcal{E}/(M_{\text{nb}}c^2)}{[1 + 2\mathcal{E}/(M_{\text{nb}}c^2)]^{1/2}}, \quad (62)$$

or $v_{\text{ej}} \approx \mathcal{E}/(M_{\text{nb}}c)$ in the non-relativistic limit. The inner ejecta with $\mathcal{E} \ll M_{\text{ext}}c^2$ would be quickly decelerated (i.e. $r_{\text{dec}} \ll r_0$) and the inner ejecta typically becomes non-relativistic at late times. Here, we focus on the refreshed forward shock emission after the inner ejecta starts the deceleration. Although the realistic behavior of the inner ejecta may be complicated at very early times, in this approximation, we may use the Sedov-Taylor solution. Then, the shock velocity is given by

$$v_s \approx 5.2 \times 10^9 \text{ cm s}^{-1} \mathcal{E}_{\text{AG},47.5}^{1/5} n_{\text{ext},3}^{-1/5} t_6^{-3/5}, \quad (63)$$

where \mathcal{E}_{AG} is the kinetic energy of the inner ejecta and n_{ext} is the external ejecta density. The external shock radius is

given by

$$r_s \approx 1.3 \times 10^{16} \text{ cm } \mathcal{E}_{\text{AG},47.5}^{1/5} n_{\text{ext},3}^{-1/5} t_6^{2/5}, \quad (64)$$

which should be larger than r_0 for our approximation to be valid. The downstream magnetic field is estimated to be

$$B_{\text{AG}} \approx (9\pi\epsilon_B n_{\text{ext}} m_p v_s^2)^{1/2} \\ \simeq 0.11 \text{ G } \mathcal{E}_{\text{AG},47.5}^{1/5} n_{\text{ext},3}^{3/10} \epsilon_{B,-2}^{1/2} t_6^{-3/5}, \quad (65)$$

where $\epsilon_B \sim 0.01$ is assumed in analogy to GRBs. We assume that electrons are accelerated with a simple power law with $dN_e/d\gamma_e \propto \gamma_e^{-s}$, where the minimum Lorentz factor of the accelerated electrons is

$$\gamma_m \approx (\zeta_e/2)(m_p/m_e)(v_s^2/c^2) \\ \simeq 8.8 \mathcal{E}_{\text{AG},47.5}^{2/5} n_{\text{ext},3}^{-2/5} \zeta_{e,-0.5} t_6^{-6/5}, \quad (66)$$

and the corresponding minimum synchrotron frequency is

$$\nu_m \approx \frac{3}{4\pi} \gamma_m^2 \frac{eB_{\text{AG}}}{m_e c} \\ \simeq 3.7 \times 10^7 \text{ Hz } \mathcal{E}_{\text{AG},47.5}^{-1/2} \epsilon_{B,-2}^{1/2} \zeta_{e,-0.5}^2 t_6^{-3}, \quad (67)$$

where ζ_e represents the combination of the acceleration efficiency (ϵ_e) and injection efficiency (f_e) at the forward shock. The synchrotron cooling Lorentz factor is

$$\gamma_c \approx \frac{6\pi m_e c}{\sigma_T B_{\text{AG}}^2 t} \\ \simeq 6.0 \times 10^4 \mathcal{E}_{\text{AG},47.5}^{-2/5} n_{\text{ext},3}^{-3/5} \epsilon_{B,-2}^{-1} t_6^{1/5}, \quad (68)$$

and the synchrotron cooling frequency is

$$\nu_c \simeq 1.7 \times 10^{15} \text{ Hz } \mathcal{E}_{\text{AG},47.5}^{-3/5} n_{\text{ext},3}^{-9/10} \epsilon_{B,-2}^{-3/2} t_6^{-1/5}. \quad (69)$$

Thus, the synchrotron spectrum is typically expected to be in the slow-cooling regime. The maximum Lorentz factor is

$$\gamma_M \approx \sqrt{\frac{9\pi v_s^2 e}{10\sigma_T B_{\text{AG}} c^2}} \\ \simeq 2.3 \times 10^7 \mathcal{E}_{\text{AG},47.5}^{1/10} n_{\text{ext},3}^{-7/20} \epsilon_{B,-2}^{-1/4} t_6^{-3/10}, \quad (70)$$

and the maximum synchrotron frequency is

$$\nu_M \simeq 2.6 \times 10^{20} \text{ Hz } \mathcal{E}_{\text{AG},47.5}^{2/5} n_{\text{ext},3}^{-2/5} t_6^{-6/5}. \quad (71)$$

The synchrotron peak flux at ν_m or ν_c is

$$F_\nu^{\text{max}} \approx \frac{0.6 f_e n_{\text{ext}} r_s^3 4\sqrt{3}\pi e^3 B_{\text{AG}}}{4\pi d^2 3m_e c^2} \\ \simeq 120 \text{ mJy } \mathcal{E}_{\text{AG},47.5}^{4/5} n_{\text{ext},3}^{7/10} \epsilon_{B,-2}^{1/2} f_e t_6^{3/5} d_{26}^{-2}. \quad (72)$$

In the slow-cooling regime, which is typically realized in all three scenarios, the synchrotron emission spectrum is

$$F_\nu^{\text{AG}} \propto \begin{cases} (\nu_m/\nu_c)^{(1-s)/2} (\nu/\nu_m)^{1/3} & (\nu \leq \nu_m) \\ (\nu/\nu_c)^{(1-s)/2} & (\nu_m < \nu \leq \nu_c) \\ (\nu/\nu_c)^{-s/2} & (\nu_c < \nu \leq \nu_M) \end{cases} \quad (73)$$

Noting that $\nu_m < \nu < \nu_c$, the radio flux is estimated to be

$$F_\nu^{\text{AG}} \sim 12 \text{ mJy } \nu_9^{1/2-s/2} \mathcal{E}_{\text{AG},47.5}^{3/10+s/2} n_{\text{ext},3}^{19/20-s/4} \\ \times \epsilon_{B,-2}^{1/4+s/4} f_e \zeta_{e,-0.5}^{-1+s} t_6^{21/10-3s/2} d_{26}^{-2}, \quad (74)$$

which implies that the radio emission may be detected by

dedicated follow-up observations with present radio facilities such as the Very Large Array (VLA). Note that the VLA flux sensitivity is $\sim 0.03\text{--}0.1$ mJy at $t \gtrsim 10^5$ s (e.g., Abbott et al. 2016), so the radio signal may be detected up to $\sim 10\text{--}100$ Mpc for $\mathcal{E}_{\text{AG}} \sim 10^{46.5}\text{--}10^{47.5}$ erg. However, one should keep in mind that star-forming galaxies are bright in the radio band. For example, the GHz radio flux of galaxies like the Milky Way is ~ 10 mJy, so the detection of weak radio signals would be possible only for nearby events. Similarly, the continuum optical flux is estimated to be

$$F_\nu^{\text{AG}} \sim 0.75 \text{ } \mu\text{Jy } \nu_{15}^{1/2-s/2} \mathcal{E}_{\text{AG},47.5}^{3/10+s/2} n_{\text{ext},3}^{19/20-s/4} \\ \times \epsilon_{B,-2}^{1/4+s/4} f_e \zeta_{e,-0.5}^{-1+s} t_6^{21/10-3s/2} d_{26}^{-2}, \quad (75)$$

which is in principle accessible with large optical telescopes such as Subaru and Keck. However, it is likely that such weak optical emission is masked by the host galaxy emission. The X-ray energy flux at $\nu > \nu_c$ is written as

$$\nu F_\nu^{\text{AG}} \sim 2.5 \times 10^{-15} \text{ erg cm}^{-2} \text{ s}^{-1} \nu_{18}^{1-s/2} \mathcal{E}_{\text{AG},47.5}^{s/2} \\ \times n_{\text{ext},3}^{1/2-s/4} \epsilon_{B,-2}^{-1/2+s/4} f_e (\zeta_e/0.4)^{-1+s} t_6^{2-3s/2} d_{26}^{-2}, \quad (76)$$

which could also be detectable by Chandra for very nearby bursts within $\sim 3\text{--}30$ Mpc, the Chandra point-source flux sensitivity being $\sim 4 \times 10^{-15}$ erg cm $^{-2}$ s $^{-1}$ with the integration time of 10^4 s. Of course, the predicted fluxes depend on the values of \mathcal{E}_{AG} .

The SSA optical depth at $\nu > \nu_m$ in the slow-cooling regime is estimated by (e.g., Panaitescu & Kumar 2004; Murase, Thompson & Ofek 2014),

$$\tau_{\text{sa}}(\nu) \approx \frac{5en_{\text{ext}}r_s}{3B_{\text{AG}}\gamma_m^5} \left(\frac{\nu}{\nu_m}\right)^{-s/2-2}. \quad (77)$$

The critical SSA frequency is determined by $\tau_{\text{sa}}(\nu_{\text{sa}}) = 1$, which leads to

$$\nu_{\text{sa}} \approx 2.5 \times 10^9 \text{ Hz } \mathcal{E}_{\text{AG},47.5}^{s/(4+s)} n_{\text{ext},3}^{(3-s/2)/(4+s)} \\ \times \epsilon_{B,-2}^{(1+s/2)/(4+s)} \zeta_{e,-0.5}^{2(s-1)/(4+s)} t_6^{(2-3s)/(4+s)}. \quad (78)$$

Thus, the SSA process can be relevant in the GHz and lower-frequency bands at early times of $t \lesssim 10^6$ s.

5 IMPLICATIONS FOR FAST RADIO BURSTS

Our paper has considered a general setup which is often used in models for FRBs and luminous SNe (including SLSNe). In this section, we focus on some implications that are specific to FRBs.

In Section 5.1, we discuss implications of the burst-in-bubble model for FRBs and constraints on their emission regions. FRBs should be attributed to coherent radio emission, which suggests that the emission radius and/or the wind Lorentz factor are large enough.

Remarkably, for some FRBs with high S/N, polarization and scattering features have been confirmed, which may indicate that the sources are in dense regions of the host galaxies, e.g., in star-forming regions (Petroff et al. 2015; Masui et al. 2015; Katz 2016). The magnetar and RNS scenarios seem consistent with this indication.

Recently, Spitler et al. (2016) reported a repeating activity of FRB 121102, while a repeatability is not observed

in other FRBs. Given the relatively small observed flux and DM, FRB 121102 may belong to a less energetic but more frequent subclass of FRBs located at a closer distance. In the burst-in-bubble model, the repeating feature could be attributed to intrinsic episodes of bursting activities or inhomogeneous interactions with the nebula. However, detailed studies of this are beyond the scope of this work.

As shown in the above, detectable HEGFs and subsequent afterglows are possible in the magnetar scenario. Thus, it is natural to ask whether the non-observation of giant flares associated with FRBs would give strong constraints on the model or not. We examine this issue in Section 5.2.

While we have focused on scenarios involving a wind bubble, FRBs may be produced by different progenitors but with the same mechanism. Indeed, at present, FRBs could be compatible with multiple physical origins. For instance, FRB 150418 is claimed to be hosted in an elliptical galaxy, where the star-formation activity would be significantly low (Keane et al. 2016). Although its association is largely disputed (e.g., Zhang 2016; Williams & Berger 2016; Akiyama & Johnson 2016), we briefly discuss some of the general implications for merger scenarios in Section 5.3.

5.1 On coherent radio emission

As mentioned above, FRB mechanisms should involve a coherent emission process. One general constraint comes from the induced-Compton scattering, although details are sensitive to the angle between a radio pulse and the relativistically moving plasma (Tanaka & Takahara 2013a). The induced-Compton scattering time is longer than the dynamical time of the photon beam when (Wilson & Rees 1978; Lyubarsky 2008)

$$\tau_{\text{ind}}^{\text{int}} \approx \frac{3\sigma_{\text{T}} n'_{\text{we}} I_{\text{FRB}} \Gamma_0 r_0}{2m_e \gamma_{\text{T}}^2 \nu^2} \lesssim 1, \quad (79)$$

where n'_{we} is the comoving lepton density of the bursting flow and γ_{T} is the temperature of electrons and positrons. The radiation intensity in the comoving frame can be connected to the observed isotropic luminosity of FRBs, $I_{\text{FRB}} \approx L_{\text{FRB}} / (64\pi^2 \Gamma_0 r^2 \nu)$. Here we assume that the size of the emission region is $l'_0 \approx \Gamma_0 c \delta t \gtrsim r_0 / (2\Gamma_0)$. The induced-Compton scattering can be neglected if

$$r_0 \gtrsim 3.8 \times 10^{16} \text{ cm } \mathcal{E}_{48}^{1/3} L_{\text{FRB},43}^{1/3} \gamma_{\text{T}}'^{-2/3} \times \Gamma_{0,6}^{-2/3} \nu_9^{-1} \Delta t_{-3}^{-1/3} \sigma_0^{-1/3} \quad (80)$$

in the magnetar scenario,

$$r_0 \gtrsim 8.3 \times 10^{14} \text{ cm } \mathcal{E}_{43}^{1/3} L_{\text{FRB},43}^{1/3} \gamma_{\text{T}}'^{-2/3} \times \Gamma_{0,6}^{-2/3} \nu_9^{-1} \Delta t_{-3}^{-1/3} \sigma_0^{-1/3} \quad (81)$$

in the RNS scenario, and

$$r_0 \gtrsim 3.8 \times 10^{15} \text{ cm } \mathcal{E}_{45}^{1/3} L_{\text{FRB},43}^{1/3} \gamma_{\text{T}}'^{-2/3} \times \Gamma_{0,6}^{-2/3} \nu_9^{-1} \Delta t_{-3}^{-1/3} \sigma_0^{-1/3} \quad (82)$$

in the MWD scenario. Thus, the FRB emission would be produced outside the light cylinder $R_{\text{lc}} \equiv c/\Omega = cP/(2\pi)$ in

all the three scenarios, unless the magnetization parameter is so large and the plasma density is small enough.

While the mechanism of the coherent emission is highly uncertain, one of the interesting possibilities is the synchrotron maser mechanism (Lyubarsky 2014). In this case, the characteristic frequency of the radio emission is estimated as $\nu_{\text{maser}} \approx (eB_* R_*) / (2^{3/2} \pi m_e c \Gamma_0)$. If $r_0 \approx R_{\text{nb}}$ is assumed, we have

$$\nu_{\text{maser}} \simeq 6.0 \times 10^7 \text{ Hz } \mathcal{E}_{48}^{-1/4} P_{i,-0.5}^{2/5} B_{*,15}^{1/2} \times M_{\text{ext},0.5}^{1/5} V_{\text{ext},8.75}^{-3/5} T_{10\text{yr}}^{-3/2} \Delta t_{-3}^{1/4} \quad (83)$$

in the magnetar scenario,

$$\nu_{\text{maser}} \simeq 4.4 \times 10^6 \text{ Hz } \mathcal{E}_{43}^{-1/4} P_{i,-3} B_{*,12.5}^{1/2} \times M_{\text{ext},0.5}^{1/2} T_{10\text{yr}}^{-3/2} \Delta t_{-3}^{1/4} \quad (84)$$

in the RNS scenario, and

$$\nu_{\text{maser}} \simeq 2.9 \times 10^4 \text{ Hz } \mathcal{E}_{45}^{-1/4} P_{i,1}^{-1/5} B_{*,9}^{11/10} \times M_{\text{ext},-3}^{1/5} V_{\text{ext},9}^{-3/5} T_{10\text{yr}}^{-6/5} \Delta t_{-3}^{1/4} \quad (85)$$

in the MWD scenario. As proposed by Lyubarsky (2014), this mechanism can be promising in the magnetar scenario. In the other two cases, the typical frequency would be smaller than the observed one, unless $r_0 \ll R_{\text{nb}}$.

5.2 Possible constraints on the magnetar scenario

So far there are no γ -ray counterpart detections associated with FRBs. Tendulkar, Kaspi & Patel (2016) summarized the fluence upper limits obtained by Konus-Wind (Aptekar et al. 1995), the Burst Alert Telescope (BAT) onboard *Swift* (Barthelmy et al. 2005), and the GRB Burst Monitor (GBM) onboard *Fermi* (Meegan et al. 2009). Assuming that these results are correct, we here convert them into upper limits of the intrinsic isotropic energy of soft gamma-rays by setting source distance in two different ways (see Table 1).

First, we simply assume a source distance of 300 Mpc. In general, an observed DM can be divided into

$$\text{DM}_{\text{obs}} = \text{DM}_{\text{MW}} + \text{DM}_{\text{halo}} + \text{DM}_{\text{IGM}} + \frac{\text{DM}_{\text{host}}}{1+z}, \quad (86)$$

where the first, second, and third term corresponds to contributions from our Galaxy, the intergalactic medium, and the host galaxy including regions close to the source, e.g., the nebula and SN ejecta, respectively. We use the NE2011 model for calculating DM_{MW} (Cordes & Lazio 2002, 2003) and set $\text{DM}_{\text{halo}} = 30 \text{ pc cm}^{-3}$. The intergalactic contribution is estimated from

$$\text{DM}_{\text{IGM}} = \frac{3cH_0 \Omega_{\text{IGM}}}{8\pi G m_p} \int_0^z \frac{(1+z') f_e(z') dz'}{[(1+z)^3 \Omega_{\text{m}} + \Omega_{\Lambda}]^{1/2}}, \quad (87)$$

with the cosmological parameters $\Omega_{\text{m}} = 0.3089$, $\Omega_{\Lambda} = 0.6911$, $\Omega_{\text{b}} = 0.0486$, and $H_0 = 67.74 \text{ km s}^{-1} \text{ Mpc}^{-1}$ (Planck Collaboration et al. 2015). We also assume $f_e = 0.88$ and $\Omega_{\text{IGM}} = 0.9 \times \Omega_{\text{b}}$. At 300 Mpc ($z = 0.0644$), $\text{DM}_{\text{IGM},300\text{Mpc}} = 65 \text{ pc cm}^{-3}$, and a significant fraction of the observed DM needs to originate from the host galaxy including the source environment such as the nebula and baryonic ejecta.

Table 1. Constraints on soft gamma-ray counterparts of FRBs. In the middle, the DM in a host galaxy (including the source environment) is estimated assuming the source distance. In the right, the source distance is estimated assuming the typical DM in elliptical galaxies.

Name	DM _{obs} ^a [pc cm ⁻³]	$\int d\varepsilon \varepsilon \phi_{\gamma}^{\max}$ ^b [erg cm ⁻²]	DM _{MW} ^c [pc cm ⁻³]	DM _{host,300Mpc} ^d [pc cm ⁻³]	$\mathcal{E}_{\gamma,300\text{Mpc}}^{\max}$ ^e [erg]	z_{ell} ^f	$\mathcal{E}_{\gamma,\text{ell}}^{\max}$ ^g [erg]
FRB 010724	375	2.0×10^{-7}	45	258	2.1×10^{48}	0.29	5.7×10^{49}
FRB 110220	944	2.0×10^{-7}	39	870	2.1×10^{48}	0.87	7.9×10^{50}
FRB 130729	861	2.0×10^{-8}	31	790	2.1×10^{47}	0.80	6.3×10^{49}
FRB 011025	790	2.0×10^{-7}	570	141	2.1×10^{48}	0.17	1.8×10^{49}
FRB 131104	779	1.0×10^{-8}	190	533	1.1×10^{47}	0.55	1.3×10^{49}
FRB 121002	1629	1.0×10^{-8}	260	1363	1.1×10^{47}	1.3	1.2×10^{50}
FRB 090625	900	1.0×10^{-8}	39	823	1.1×10^{47}	0.83	3.8×10^{49}
FRB 110703	1104	1.0×10^{-8}	33	1046	1.1×10^{47}	1.0	6.1×10^{49}
FRB 130626	952	2.0×10^{-8}	54	862	2.1×10^{47}	0.86	7.7×10^{49}
FRB 140514	563	2.0×10^{-8}	37	466	2.1×10^{47}	0.49	2.0×10^{49}
FRB 130628	470	1.0×10^{-8}	53	350	1.1×10^{47}	0.38	5.3×10^{48}
FRB 121102	557	2.0×10^{-8}	190	297	2.1×10^{47}	0.33	7.6×10^{48}
FRB 110626	723	2.0×10^{-7}	56	616	2.1×10^{48}	0.63	3.6×10^{50}
FRB 120127	553	2.0×10^{-8}	33	460	2.1×10^{47}	0.48	1.9×10^{49}

^{a,b} Observed dispersion measures and upper limit on the soft gamma-ray fluence (Tendulkar, Kaspi & Patel 2016, and references therein). ^c Calculated dispersion measures in our Galaxy based on the NE2001 model (Cordes & Lazio 2002, 2003). ^{d,e} Calculated dispersion measures in the host galaxy and upper limit on the intrinsic soft gamma-ray radiation energy with the assumption that the distance is 300 Mpc from the Earth. ^{f,g} Calculated source redshifts and upper limits on the intrinsic soft gamma-ray radiation energy with the assumption that the host galaxy is elliptical.

The estimated upper limits of the intrinsic isotropic energy of soft gamma-rays ranges from $\mathcal{E}_{\gamma,300\text{Mpc}}^{\max} \sim 10^{47} - 10^{48}$ erg, which is larger than the energy of the giant flare from SGR 1806-20 but close to values expected in the hyper-flare scenario. Thus, if soft gamma-ray emission is produced concurrently with magnetic reconnections (Thompson & Duncan 1995, 2001; Gill & Heyl 2010; Elenbaas et al. 2016), the absence of correlations between FRBs and hyper-flares can constrain the magnetar scenario (if the soft gamma-ray emission is ubiquitous). Based on these results, we encourage further soft gamma-ray searches especially with *Swift*. Possible detection of FRB counterparts with gamma-ray energies exceeding values of Eq. (33) can exclude magnetar and MWD models, in which the magnetic energy of remnants such as NSs and WDs is used. Non-detection is also useful. If the nebula and ejecta contribute more significantly to the DM, the limits would become tighter, so that the hyper-flare model is disfavored. This is because the distance to FRBs would need to be smaller than ~ 300 Mpc in this case. Of course, an association with a dimmer class of magnetically-induced bursts is not ruled out, even for an FRB distance of $d \lesssim 300$ Mpc.

5.3 Possible constraints on merger scenarios

Our burst-in-bubble model is applicable not only to models involving a SN explosion but also to some models involving compact mergers, as considered in the MWD scenario. Even in merger scenarios, mass ejection is expected around the coalescence time. The total ejected mass is rather uncertain and depends on the binary parameters; for example, $M_{\text{ext}} \sim 10^{-5} - 10^{-2} M_{\odot}$ for a NS-NS binary based on numerical simulations (see, e.g., Kiuchi et al. 2014; Sekiguchi et al. 2015). The ejecta velocity is expected to be $V_{\text{ext}} \approx 0.3c$ for a NS-NS merger and $V_{\text{ext}} \approx 0.06c$ for a WD-

WD merger. However, as long as we consider FRB emission at early times with $T \lesssim 1$ yr, the corresponding electron density is high enough to prevent FRB emission from escaping the system. Thus, FRBs need to be produced as precursors before the actual merger (e.g., Totani 2013; Lyutikov 2013). Alternatively, since the mass ejection in general occurs in a highly anisotropic manner, FRBs may be possible when the magnetic dissipation occurs outside the ejecta, if relativistic Poynting-dominated outflows get ahead of the slower ejecta (e.g., Kashiyama, Ioka & Mészáros 2013).

In such situations, contributions of the source environment to DM_{host} are expected to be small. Assuming that DM_{host} is dominated by the host galaxy contribution, in Table 1, we use DM_{host} = 30 pc cm⁻³ that is typical for elliptical galaxies. Then, the redshifts of the host galaxies are estimated from Eq. (86) as $z_{\text{ell}} \sim 0.2 - 1$. We finally derive upper limits on the intrinsic isotropic energy of the soft γ -rays ranging from $\mathcal{E}_{\gamma,\text{ell}}^{\max} \sim 5 \times 10^{48}$ erg to $\mathcal{E}_{\gamma,\text{ell}}^{\max} \sim 5 \times 10^{50}$ erg. This would exclude an association of an FRB with on-axis short GRBs, at least for several events.

In merger scenarios, the mass ejection leads to a broadband afterglow emission that may be detectable with dedicated follow-up observations (Niino, Totani & Okumura 2014) (and see also Yi, Gao & Zhang 2014, for the discussion on possible afterglows), which has also been of interest for giving rise to counterparts of gravitational waves. The deceleration time of the merger ejecta is estimated to be $T_{\text{ST}} \simeq 2.1 \text{ yr } M_{\text{ext}}^{1/3} n_{\text{ism}}^{-1/3} V_{\text{ext},10}^{-1}$. In the case of the dynamical ejecta of a NS-NS merger, the peak flux is in the range $\sim 10^{26-28} \text{ erg s}^{-1} \text{ Hz}^{-1}$ in the $\sim 0.1 - 1$ GHz bands (e.g., Hotokezaka & Piran 2015, and references therein), and the emission is slower and dimmer for WD-WD merger with a slower ejecta velocity. The radio emission is stronger if a long-lived magnetar exists (Metzger & Bower 2014), which may already be ruled out for the two kilonova/macronova

candidates (Horesh et al. 2016). More rapid radio afterglows fading within 100 days can be also produced if a short GRB jet is launched after the NS-NS merger. In any of the references mentioned above, the radio signature is qualitatively different from the one considered in the present work.

Finally, we note that merger scenarios discussed above cannot explain a repeating FRB such as that reported by Spitler et al. (2016). However, as argued by many authors, FRBs may have multiple origins and these models could still be viable to explain the other FRBs.

6 SUMMARY

We have studied the various roles played by a tenuous wind bubble formed by relativistic winds from a rotating compact remnant such as a NS or WD. Such a setup is commonly expected for young NSs and WDs after stellar core-collapse or mergers, respectively, and it is often employed in models for FRBs as well as SLSNe and GRBs. Throughout this paper, we considered three examples, (a) the magnetar scenario, (b) the RNS scenario, and (c) the MWD scenario. Our results are summarized as follows.

(i) First, we calculated the quasi-steady nebular emission of extragalactic pulsar wind nebulae, based on parameters of Galactic pulsar wind nebulae. The nebula’s emission itself is difficult to detect in the magnetar and MWD scenarios. On the other hand, in the RNS scenario, the GHz radio flux at $T \sim 100$ yr can be ~ 1 mJy for an event at $d \sim 100$ Mpc, and the related emission is detectable with present radio telescopes such as VLA, SMA, and ALMA. In particular, higher-frequency emission in the sub-mm band would provide a way to test pulsar-driven SN model and FRBs. Then, we studied the effects of the nebula’s emission on the attenuation of high-energy gamma-rays and radio waves. We showed that the escape of high-energy gamma-rays, including TeV photons, is possible in all three scenarios. The radio emission can be severely absorbed in the nebula and in the external ejecta, but the system can be transparent to GHz radio waves at time $T \gtrsim 10 - 100$ yr. Thus, if FRBs originate from magnetars or RNSs, their age is expected to be $T \gtrsim 10 - 100$ yr.

(ii) Second, we suggested HEGFs caused by possible magnetic dissipation in the nebula. An impulsive relativistic outflow, which propagates in the wind and is quickly decelerated by interactions with the nebula, can boost a population of pre-existing non-thermal particles. The duration HEGFs may be as short as milliseconds but can also be longer, depending on the expansion of the outflow. For the magnetar scenario, HEGFs from the forward shock may occur in the fast-cooling regime, and TeV gamma-rays from nearby events with $\lesssim 10 - 100$ Mpc may be detected with HAWC. CTA could detect more distant HEGFs up to $\sim 0.1 - 1$ Gpc although its field-of-view is much smaller. On the other hand, only a fraction of the energy would be converted into gamma-rays in the RNS and MWD scenarios, so detecting HEGFs from these would be more challenging. We also considered possible flaring emission from the reverse shock, which may lead to additional gamma-ray emission.

(iii) Third, we considered the subsequent afterglow emission following HEGFs and possible FRBs. In the mag-

netar scenario, the associated radio emission from the external forward shock is detectable with dedicated follow-up observations, for a nearby event at $\sim 10 - 100$ Mpc.

(iv) While our setup is not sensitive to details of the FRB mechanism, we discussed specific implications for FRBs. The induced-Compton scattering implies that the emission regions are far beyond the light cylinder for the burst-in-bubble models considered here. We also considered limits on hyper-flares expected in the magnetar scenario. The limits are consistent with the model, as long as they do not exceed $\mathcal{E}_{\text{mag}} \sim 10^{48}$ erg. But these limits should be tighter for younger nebulae since electrons and positrons in the nebula and/or ejecta can significantly contribute to the DM.

ACKNOWLEDGMENTS

K. M. thanks Hiroya Yamaguchi for useful discussion. K. K. is supported by NASA through Einstein Postdoctoral Fellowship grant number PF4-150123 awarded by the Chandra X-ray Center, operated by the Smithsonian Astrophysical Observatory for NASA under contract NAS8-03060. P. M. acknowledges partial support by NASA NNX13AH50G.

APPENDIX A: ON THE DETECTION OF QUASI-STEADY NEBULA EMISSION

In this Appendix, we briefly discuss radio signatures of the quasi-steady nebular emission described in Section 2.2. For the calculations, we use the code developed by Murase et al. (2015), taking also into account the effect of residual electron-positron pairs, which are relevant for the emission after the spin-down time. Our results on the light curves are shown in Figs. 11-13.

In the magnetar scenario, the nebular synchrotron emission is too weak to be detected at late times, but embryonic emission (at $T \lesssim$ a few yr) can be of interest at high frequencies. However, as shown in Section 2.3, both the radio and sub-mm emission will be masked by the free-free absorption for our parameter set, so only X-rays and high-energy (GeV-TeV) gamma-rays would be detectable (Murase et al. 2015). On the other hand, for our parameters of the RNS scenario, the GHz radio flux around $T \sim 100$ yr is $F_{\nu}^{\text{nb}} \sim 1$ mJy $d_{26.5}^{-2}$ (see the middle panel of Figs. 2 and 12), so RNS at $\lesssim 100$ Mpc nebulae would be detectable with current radio telescopes.

Our results shown in Figs. 2 and 12 imply that searching for radio counterparts of pulsar-driven SNe, including SLSNe, is relevant especially at higher frequencies, where the absorption is less relevant. The Atacama Large Millimeter/sub-millimeter Array (ALMA) may detect the nebular emission from the RNS. Although the detectability is sensitive to P (that increases at $T > T_{\text{sd}}$), for our parameter set of the RNS scenario, the 100 GHz radio flux around $T \sim 10$ yr reaches $F_{\nu}^{\text{nb}} \sim 0.8$ mJy $d_{27.5}^{-2}$, which exceeds the ALMA sensitivity of ~ 0.01 mJy as well as that of the SMA array.

The pulsar-driven SN model requires that almost all

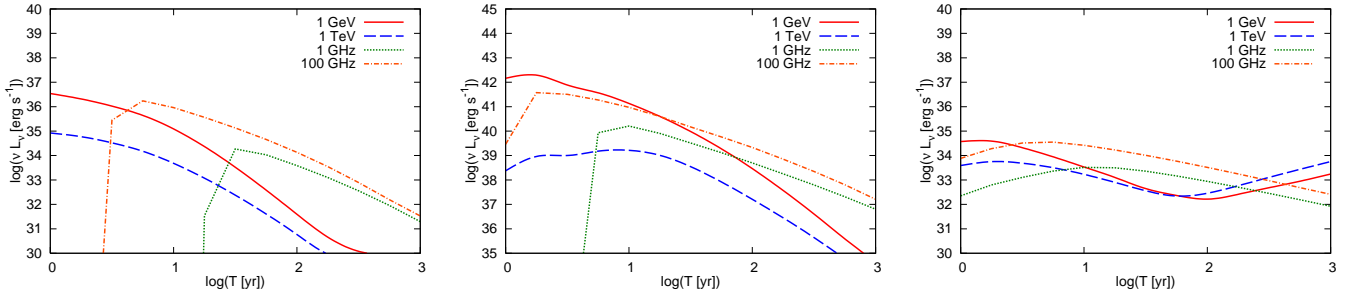


Figure A1. Corresponding to Fig. 2, light curves of radio and gamma-ray emission from a very young nebula are shown for the magnetar scenario (left panel), RNS scenario (middle panel), and MWD scenario (right panel).

the spin-down energy is dissipated, and a significant fraction of that energy needs to be converted into the observed SN emission. Thus, the radio and sub-mm signals can be used as relevant probes. The rate of SLSNe is only $\sim 10 \text{ Gpc}^{-3} \text{ yr}^{-1}$ (Gal-Yam 2012). Thus, the number of their radio counterparts within 100 Mpc with $T \lesssim 10 - 100 \text{ yr}$ is about 0.3 – 3, so non-detections with radio surveys are not constraining. However, future dedicated follow-up surveys should provide a powerful test. This is especially the case for sub-mm telescopes, which have a small field of view.

The quasi-steady nebular emission can be more relevant for testing models for FRBs. The FRB rate is $\sim 10^4 \text{ Gpc}^{-3} \text{ yr}^{-1}$, leading to the number of their radio counterparts within 100 Mpc with $T \lesssim 10 - 100 \text{ yr}$ being about 300 – 3000. This is especially the case for a RNS model such that the FRBs are powered by the spin-down luminosity rather than the magnetic energy. Note that the rotation period increases after the spin-down time T_{sd} , and the spin-down luminosity for our RNS parameters is $L_{\text{sd}} \sim 10^{43} \text{ erg s}^{-1}$ at $T \sim 10 \text{ yr}$, which is comparable to the observed FRB luminosity. We expect that the RNS model for FRBs is strongly constrained for RNSs with $P_i \sim 1 - 10 \text{ ms}$, because of the absence of such luminous transients in the radio sky (as long as a significant fraction of the spin-down energy is dissipated around the nebula). Note that such nebular emission should be non-thermal, which can be discriminated from Galactic thermal sources. Discriminating them from active galactic nuclei would be more difficult, and it would need information on counterparts at other wavelengths and/or variability time scales.

APPENDIX B: COMMENTS ON FRB 121102

Recently, a radio counterpart of FRB 121102 was reported via the observations by the VLA and the European VLBI Network (EVN), respectively (Chatterjee et al. 2017; Marcote et al. 2017). Tendulkar et al. (2017) identified their host galaxy with redshift $z \approx 0.19$. For the first time, they have established an FRB as a cosmological event. They also found a quasi-steady radio source with an observed flux of $\sim 0.2 \text{ mJy}$ at $\sim 1 - 10 \text{ GHz}$, which corresponds to a luminosity of $\sim 10^{39} \text{ erg s}^{-1}$. Remarkably, this is consistent with our model, as seen in the middle panel of our Figure 2 for the RNS scenario. Indeed, the parameters,

$B_* = 10^{12.5} \text{ G}$ and $P_i = 1 \text{ ms}$, lie in the allowed parameter space shown in Kashiyama & Murase (2017). Note that SSA is the most important process that suppresses the synchrotron flux at sufficiently low frequencies. Also, in general, the energy source of FRB emission itself does not have to be rotation energy that is responsible for the nebular emission (e.g., Falcke & Rezzolla 2014).

While other possibilities such as emission from low-luminosity active galactic nuclei are not ruled out, this discovery encourages our proposal of follow-up observations of pulsar-driven SN candidates, especially at submm frequencies. SLSNe are of particular interest, where $\sim 1 - 10 \text{ yr}$ time scale observations at high frequencies are crucial. With the MHD-motivated spin-down formula, Kashiyama et al. (2016) showed that SLSNe favor $B_* \sim 10^{13} - 10^{14} \text{ G}$ and $P_i \sim$ a few ms (see Figure 6 of Kashiyama et al. 2016). The parameters favored by FRB 121102 are not too far from them, so searches for radio counterparts will give us important information on the relationship between FRBs and pulsar-driven SNe, including SLSNe. Also, as suggested by Kashiyama et al. (2016) (see their Figure 9), “hard” X-rays should also serve as promising signals for the parameters that may account for SLSNe and FRBs.

REFERENCES

- Abbott B. P. et al., 2016, arXiv:1602.08492
 Abeyssekara A. U. et al., 2013, *Astroparticle Physics*, 50, 26
 Akiyama K., Johnson M. D., 2016, arXiv:1603.04880
 Aptekar R. L. et al., 1995, *Space Sci. Rev.*, 71, 265
 Barthelmy S. D. et al., 2005, *Space Sci. Rev.*, 120, 143
 Blackman E. G., Yi I., 1998, *ApJL*, 498, L31
 Blondin J. M., Chevalier R. A., Frierson D. M., 2001, *ApJ*, 563, 806
 Bühler R., Blandford R., 2014, *Reports on Progress in Physics*, 77, 066901
 Burke-Spolaor S., Bannister K. W., 2014, *ApJ*, 792, 19
 Champion D. J. et al., 2015, arXiv:1511.07746
 Chatterjee S. et al., 2017, *Nature*, 541, 58
 Chevalier R. A., 1977, in *Astrophysics and Space Science Library*, Vol. 66, Supernovae, Schramm D. N., ed., p. 53
 Chevalier R. A., 2005, *ApJ*, 619, 839
 Connor L., Sievers J., Pen U.-L., 2016, *MNRAS*, 458, L19
 Cordes J. M., Lazio T. J. W., 2002, astro-ph/0207156
 Cordes J. M., Lazio T. J. W., 2003, astro-ph/0301598

- Cordes J. M., Wasserman I., 2016, *MNRAS*, 457, 232
- Dai Z. G., Lu T., 1998, *A&A*, 333, L87
- Elenbaas C., Watts A. L., Turolla R., Heyl J. S., 2016, *MNRAS*, 456, 3282
- Falcke H., Rezzolla L., 2014, *A&A*, 562, A137
- Fang K., Kotera K., Murase K., Olinto A. V., 2014, *Phys. Rev. D*, 90, 103005
- Faucher-Giguère C.-A., Kaspi V. M., 2006, *ApJ*, 643, 332
- Gaensler B. M. et al., 2005, *Nature*, 434, 1104
- Gaensler B. M., Slane P. O., 2006, *ARA&A*, 44, 17
- Gal-Yam A., 2012, *Science*, 337, 927
- Gao H., Ding X., Wu X.-F., Dai Z.-G., Zhang B., 2015, *ApJ*, 807, 163
- Ghisellini G., Svensson R., 1991, *MNRAS*, 252, 313
- Gill R., Heyl J. S., 2010, *MNRAS*, 407, 1926
- Goldreich P., Julian W. H., 1969, *ApJ*, 157, 869
- Granot J. et al., 2006, *ApJ*, 638, 391
- Gruzinov A., 2005, *Physical Review Letters*, 94, 021101
- Hamilton A. J. S., Sarazin C. L., 1984, *ApJ*, 287, 282
- Horesh A., Hotokezaka K., Piran T., Nakar E., Hancock P., 2016, *ApJL*, 819, L22
- Hotokezaka K., Piran T., 2015, *MNRAS*, 450, 1430
- Inoue S., 2004, *MNRAS*, 348, 999
- Inoue S., Guetta D., Pacini F., 2003, *ApJ*, 583, 379
- Ioka K., 2003, *ApJL*, 598, L79
- Ji S. et al., 2013, *ApJ*, 773, 136
- Kakuwa J., Murase K., Toma K., Inoue S., Yamazaki R., Ioka K., 2012, *MNRAS*, 425, 514
- Kasen D., Bildsten L., 2010, *ApJ*, 717, 245
- Kashiyama K., Ioka K., Kawanaka N., 2011, *Phys. Rev. D*, 83, 023002
- Kashiyama K., Ioka K., Mészáros P., 2013, *ApJL*, 776, L39
- Kashiyama K., Murase K., 2017, *arXiv:1701.04815*
- Kashiyama K., Murase K., Bartos I., Kiuchi K., Margutti R., 2016, *ApJ*, 818, 94
- Katz J. I., 1982, *ApJ*, 260, 371
- Katz J. I., 2014, *Phys. Rev. D*, 89, 103009
- Katz J. I., 2016, *ApJ*, 818, 19
- Keane E. F. et al., 2016, *Nature*, 530, 453
- Keane E. F., Petroff E., 2015, *MNRAS*, 447, 2852
- Keane E. F., Stappers B. W., Kramer M., Lyne A. G., 2012, *MNRAS*, 425, L71
- Kennel C. F., Coroniti F. V., 1984, *ApJ*, 283, 710
- Kisaka S., Ioka K., Nakar E., 2016, *ApJ*, 818, 104
- Kisaka S., Ioka K., Takami H., 2015, *ApJ*, 802, 119
- Kiuchi K., Kyutoku K., Sekiguchi Y., Shibata M., Wada T., 2014, *Phys. Rev. D*, 90, 041502
- Kohri K., Ohira Y., Ioka K., 2012, *MNRAS*, 424, 2249
- Komissarov S. S., 2013, *MNRAS*, 428, 2459
- Komissarov S. S., Lyutikov M., 2011, *MNRAS*, 414, 2017
- Kotera K., Phinney E. S., Olinto A. V., 2013, *MNRAS*, 432, 3228
- Kulkarni S. R., Ofek E. O., Neill J. D., Zheng Z., Juric M., 2014, *ApJ*, 797, 70
- Law C. J. et al., 2015, *ApJ*, 807, 16
- Loeb A., Shvartzvald Y., Maoz D., 2014, *MNRAS*, 439, L46
- Lorimer D. R., Bailes M., McLaughlin M. A., Narkevic D. J., Crawford F., 2007, *Science*, 318, 777
- Lyubarsky Y., 2008, *ApJ*, 682, 1443
- Lyubarsky Y., 2014, *MNRAS*, 442, L9
- Lyutikov M., 2013, *ApJ*, 768, 63
- Maeda K. et al., 2007, *ApJ*, 666, 1069
- Maoz D. et al., 2015, *MNRAS*, 454, 2183
- Marcote B. et al., 2017, *ApJL*, 834, L8
- Masui K. et al., 2015, *Nature*, 528, 523
- Meegan C. et al., 2009, *ApJ*, 702, 791
- Metzger B. D., Bower G. C., 2014, *MNRAS*, 437, 1821
- Michel F. C., 1969, *ApJ*, 158, 727
- Murase K., Kashiyama K., Kiuchi K., Bartos I., 2015, *ApJ*, 805, 82
- Murase K., Mészáros P., Zhang B., 2009, *Phys. Rev. D*, 79, 103001
- Murase K., Thompson T. A., Ofek E. O., 2014, *MNRAS*, 440, 2528
- Niino Y., Totani T., Okumura J. E., 2014, *PASJ*, 66, L9
- Panaitescu A., Kumar P., 2004, *MNRAS*, 353, 511
- Petroff E. et al., 2015, *MNRAS*, 447, 246
- Planck Collaboration et al., 2015, *arXiv:1502.01589*
- Popov S. B., Postnov K. A., 2010, in *Evolution of Cosmic Objects through their Physical Activity*, Harutyunian H. A., Mickaelian A. M., Terzian Y., eds., pp. 129–132
- Ravi V., Shannon R. M., Jameson A., 2015, *ApJL*, 799, L5
- Rees M. J., Gunn J. E., 1974, *MNRAS*, 167, 1
- Sekiguchi Y., Kiuchi K., Kyutoku K., Shibata M., 2015, *Phys. Rev. D*, 91, 064059
- Sironi L., Spitkovsky A., 2009, *ApJ*, 698, 1523
- Spitkovsky A., 2006, *ApJL*, 648, L51
- Spitler L. G. et al., 2014, *ApJ*, 790, 101
- Spitler L. G. et al., 2016, *Nature*, 531, 202
- Tanaka S. J., Takahara F., 2010, *ApJ*, 715, 1248
- Tanaka S. J., Takahara F., 2013a, *Progress of Theoretical and Experimental Physics*, 2013, 123E01
- Tanaka S. J., Takahara F., 2013b, *MNRAS*, 429, 2945
- Tchekhovskoy A., Spitkovsky A., Li J. G., 2013, *MNRAS*, 435, L1
- Tendulkar S. P. et al., 2017, *ApJL*, 834, L7
- Tendulkar S. P., Kaspi V. M., Patel C., 2016, *arXiv:1602.02188*
- Thompson C., 1994, *MNRAS*, 270, 480
- Thompson C., Duncan R. C., 1995, *MNRAS*, 275, 255
- Thompson C., Duncan R. C., 2001, *ApJ*, 561, 980
- Thompson T. A., Chang P., Quataert E., 2004, *ApJ*, 611, 380
- Thornton D. et al., 2013, *Science*, 341, 53
- Totani T., 2013, *PASJ*, 65
- Usov V. V., 1992, *Nature*, 357, 472
- Vietri M., Stella L., 1998, *ApJL*, 507, L45
- Williams P. K. G., Berger E., 2016, *arXiv:1602.08434*
- Wilson D. B., Rees M. J., 1978, *MNRAS*, 185, 297
- Wosley S. E., 2010, *ApJL*, 719, L204
- Yang Y.-P., Zhang B., Dai Z.-G., 2016, *ApJL*, 819, L12
- Yi S.-X., Gao H., Zhang B., 2014, *ApJL*, 792, L21
- Zhang B., 2014, *ApJL*, 780, L21
- Zhang B., 2016, *arXiv:1602.08086*
- Zhang B., Mészáros P., 2001, *ApJL*, 552, L35

This paper has been typeset from a \TeX / \LaTeX file prepared by the author.